Available online at www.sciencedirect.com

ScienceDirect

Underground Space 26 (2026) 82–105

www.keaipublishing.com/undsp

Evolution of mechanical properties of shield tunnels induced by water-soil gushing

Xiao-Chuang Xie [a], Dong-Mei Zhang [a,b,*], Ming-Liang Zhou [a]

[a] *Department of Geotechnical Engineering, College of Civil Engineering, Tongji University, Shanghai 200092, China*
[b] *State Key Laboratory of Disaster Reduction in Civil Engineering, Tongji University, Shanghai 200092, China*

Received 27 September 2024; received in revised form 14 December 2024; accepted 18 December 2024
Available online 24 October 2025

Abstract

Water and soil gushing in shield tunnels pose a significant risk to tunnel structure safety. However, it is challenging to fully capture the evolution of the mechanical response of tunnel structures due to the limitations of conventional numerical methods in simulating large soil deformations around the tunnel due to gushing. This paper developed a coupled material point method (MPM) and finite element method (FEM) approach for water and soil gushing, where MPM was for modelling the soil deformation and FEM was for modelling the tunnel response. The developed approach was utilized to conduct the gushing-induced large deformation analyses and generate the varying soil and water pressures acting on the tunnel lining. Meanwhile, structural internal forces and joint deformations were identified based on the load-structure method. The findings suggest that the gushing process can be categorized into three stages: initial developing, rapid developing, and stable developing stages. The soil and water pressures around the gushing point decreased abruptly during the "rapid developing stage", but the soil pressures on the tunnel crown and tunnel invert increase, causing a sharp rise in the bending moment of the lining and severe joint deformations, particularly at joints No. 2 and No. 3. Finally, the parametric analyses show that a lower gushing location, deeper tunnel depth, and higher soil shear strength will all exacerbate the influence of water-soil gushing on tunnel structural response, due to variations in the soil and water pressures acting on the tunnel lining throughout the whole process of gushing. These findings underscore the importance of revealing the evolution of tunnel responses to water-soil gushing for maintaining tunnel safety.

Keywords: Water-soil gushing; Shield tunnel; Mechanical response; Joint deformation

1 Introduction

As underground transportation networks rapidly expand, the shield tunnelling method has become increasingly prevalent due to its high efficiency and minimal environmental disruption. Shield tunnels are assembled from concrete linings, and inherently consist of a large number of segmental joints, which are particularly susceptible to water inflow and even the accompanying loss of soil particles (Lin et al., 2024; Long & Tan, 2020; Tan & Lu, 2017; Wallis, 2002; Wang et al., 2024; Wu et al., 2014). As illustrated in Fig. 1(a), this infiltration of water and soil particles can critically undermine the long-term structural integrity and operational safety of the tunnel (Mair, 2008; Wongsaroj et al., 2007; Yang et al., 2022; Yoo, 2017; D. Zhang et al., 2015). Defective linings and enlarged segmental joints can cause more severe water-soil gushing, with large amounts of soil and water gushing into the tunnel, resulting in dramatic consequences and posing a considerable risk to public safety, as shown in Fig. 1(b). For instance, Huang et al. (2020) investigated a sudden water-soil gushing incident at a metro line in Tianjin, China, that led to substantial soil deformation around the connecting

* Corresponding author at: Department of Geotechnical Engineering, College of Civil Engineering, Tongji University, Shanghai 200092, China.
E-mail address: dmzhang@tongji.edu.cn (D.-M. Zhang).
Peer review under the responsibility of Tongji University

https://doi.org/10.1016/j.undsp.2024.12.008
2467-9674/© 2025 Tongji University. Publishing Services by Elsevier B.V. on behalf of KeAi Communications Co. Ltd.
This is an open access article under the CC BY-NC-ND license (http://creativecommons.org/licenses/by-nc-nd/4.0/).

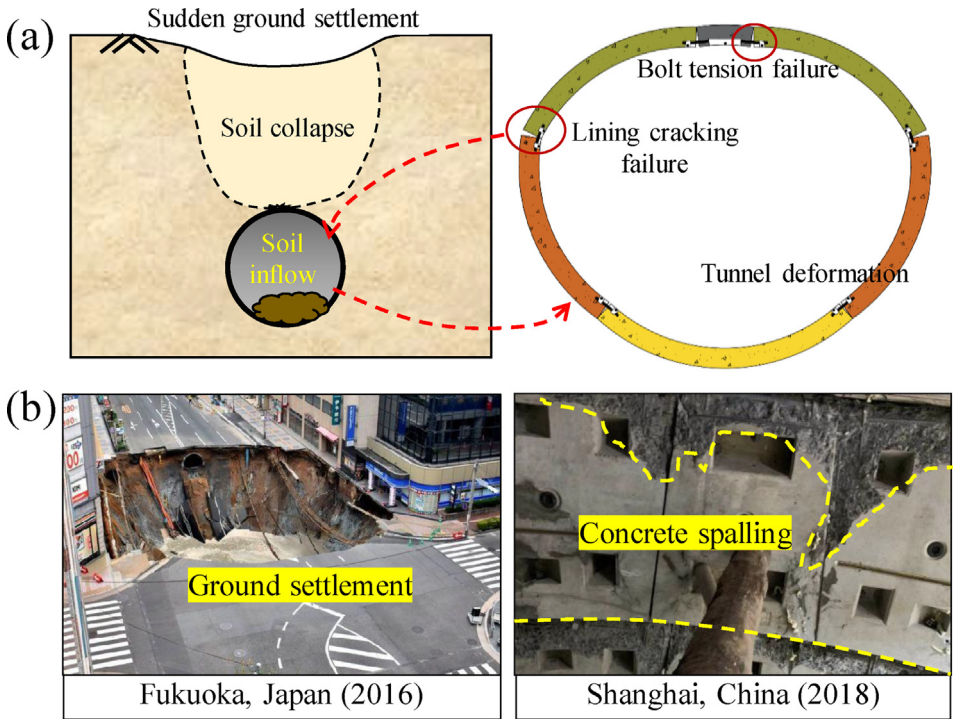

Fig. 1. Consequence of water and soil inflow in the tunnel.

passage and significant damage to the tunnel linings. Zhang et al. (2021) reported a water-soil gushing incident at a Shanghai Metro Line, highlighting the grave risks associated with this category of hazard, such as sudden ground settlement and lining cracking failure, which would substantially degrade the durability of the tunnel lining (Rabczuk & Belytschko, 2004; Rabczuk et al., 2010; Sun et al., 2019; Y. Zhang et al., 2020, 2015; Zhang & Mang, 2020; Zhang & Zhuang, 2018, 2019). These cases underscore the critical need for stringent monitoring, early warning systems, and effective prevention strategies to address water and soil gushing in tunnels.

Some researchers have adopted numerical methods to study the effects of water inflow on tunnel responses as well as surrounding soil deformation. D. Zhang et al. (2015) studied the responses of the soil layers and tunnel structures to partial leakage at segmental joints in saturated clay, while Yoo (2017) conducted numerical analyses on the structural performance underlining leakage conditions. Despite these efforts, there have been a few studies focusing on the consequences of soil inflow on tunnel linings (Lin et al., 2022; Meguid & Dang, 2009; Wang et al., 2014). For instance, Qin et al. (2022) examined the formation of erosion voids in the surrounding soil and their influences on tunnel lining using finite element method (FEM). However, these studies assume the presence of idealized arc-shaped soil cavities around tunnels and primarily pay attention to the differences in tunnel behaviour before and after the creation of erosion voids, overlooking the development of tunnel responses during the whole water-soil gushing process (Lin et al., 2023). Although Zhang et al. (2022) explored the effects of seepage erosion around shield tunnels at a representative elementary scale using the discrete element method (DEM), its use for large-scale geotechnical structures is limited by its computational demands. This highlights the urgent need for alternative numerical methods capable of accurately reproducing the complex interactions between substantial soil deformations and tunnel structures during water-soil gushing.

Material point method (MPM) is particularly effective for simulating large deformation issues and has been applied to various geotechnical problems, including slope failures (Ceccato et al., 2024; Lu et al., 2024; Ng et al., 2024; Soga et al., 2016), soil-penetration problems (Ceccato et al., 2020), and tunnelling (Fern, 2019). Moreover, for both saturated and unsaturated soils, multi-phase MPM formulations were developed (Bandara & Soga, 2015; Ceccato et al., 2021; Jassim et al., 2013). In addressing the soil-structure interaction, several methods within MPM, such as level-set based contact algorithms (Zhao et al., 2023), interface elements (Vermeer et al., 2009), and multi-velocity field formulations (Ma et al., 2014), have been developed. The nodal contact algorithm (Bardenhagen et al., 2001) is among the most widely used due to its efficiency in capturing interactions between solids and granular material shearing (Ceccato et al., 2017). However, many of these studies assumed rigid structures, thus neglecting the critical aspects of stress and strain within the tunnel structures, which are essential in this study.

Although MPM is advantageous for modelling substantial soil deformations, its computational efficiency and accuracy are often lower than FEM when dealing with

small-strain problems (Lei et al., 2022; Lian et al., 2011). Combining MPM with FEM has attracted increasing attention for problems involving both small and large deformations. The material point finite element method (MPFEM) (Zhang et al., 2006), and the coupled finite element material point method (CFEMPM) (Chen et al., 2015) have been developed for applications such as hyper-velocity impacts and fluid–structure interactions. Nonetheless, the combined use of MPM and FEM for geotechnical problems involving soil-structure interactions and large soil deformations remains relatively underexplored, particularly in the problem of water and soil gushing surrounding tunnels.

This paper presents a comprehensive investigation into the effects of water-soil gushing on tunnel structures by introducing a unidirectional MPM–FEM computational framework. A two-phase single-point MPM formulation is used to effectively address the complexities of substantial soil deformations caused by gushing and quantify the development of soil and water pressure acting on the lining surface. By using a data transmission module, the soil and water pressures can be immediately applied as external loads in an FEM model for solving the response of tunnels with segment joints. To validate the practicality and reliability of the proposed MPM–FEM approach, a case study was conducted, which demonstrated the effectiveness of the proposed approach in capturing the mechanical evolutions of tunnel structures due to water-soil gushing. Finally, a parametric analysis was performed to explore the effects of various factors, including gushing location, tunnel burial depth, and soil properties, on the internal forces of the lining and the structural deformation. This study provides new insights into the evolution of tunnel responses to water-soil gushing that have never been discussed in earlier studies.

2 Framework of water-soil gushing modelling

As depicted in Fig. 1, the substantial soil deformation resulting from water-soil gushing can lead to pronounced tunnel deflection and potentially severe joint failure, characterizing a complex, large deformation and nonlinear problem. The critical challenge lies in accurately simulating the large soil deformations surrounding the shield tunnel and the nonlinear deflections of the tunnel induced by the dynamic soil and water pressures acting on the concrete lining. To achieve this purpose, an MPM–FEM numerical approach is presented here to investigate the mechanical responses of tunnels caused by the gushing in water-rich layers. The numerical approach consists of two main steps: the MPM modelling of soil deformation and the FEM modelling of tunnel behaviour.

2.1 MPM modelling of soil behaviour

The MPM is a kind of numerical method which incorporates the strengths of the Lagrangian and Eulerian descriptions, for instance, high computational efficiency and no mesh distortion (Fern et al., 2019; Sulsky et al., 1995). In MPM, a set of material points (MPs) is used to model arbitrarily large deformations of an object. The MPs carry all data including stress, strain, velocity, density and other material properties, and update the information in conjunction with a set of background grids, in which the momentum equivalent is calculated (Kafaji, 2013). By resetting the computational mesh after each step, MPM avoids mesh distortion issues commonly encountered in FEM. Figure 2 presents a scheme of the MPM approach. In the two-phase single-point MPM, every MP serves as a subdomain of the saturated soil and contains data for both solid and liquid phases. The momentum equation for the mixture can be written as

$$(1-n)\rho_s\frac{d\boldsymbol{v}_s}{dt}+n\rho_l\frac{d\boldsymbol{v}_l}{dt}=\nabla\boldsymbol{\sigma}+\bar{\rho}\,\boldsymbol{g}, \tag{1}$$

where n is the porosity; $\boldsymbol{v}_s$ and $\boldsymbol{v}_l$ are the velocity vectors of the solid phase and the liquid phase, respectively; ρ_s and ρ_l are the densities of the soil and water, respectively; $\bar{\rho}=(1-n)\rho_s+n\rho_l$ is the density of the mixture; $\boldsymbol{g}$ is the gravity vector; $\boldsymbol{\sigma}$ is the soil stress tensor.

The momentum equation of the liquid phase is given as

$$\rho_l\frac{d\boldsymbol{v}_l}{dt}=\nabla p_l-\frac{n\rho_l\boldsymbol{g}}{k_l}(\boldsymbol{v}_l-\boldsymbol{v}_s)+\rho_l\boldsymbol{g}, \tag{2}$$

where k_l is the Darcy permeability, and p_l is the pore pressure. More details could be obtained from the publications (Ceccato et al., 2016; Jassim et al., 2013).

As illustrated in Fig. 2, the MPM modelling process within a single time increment comprises four steps. Initially, all information in MPs is mapped to the computational grids. Next, the momentum conservations are computed at the nodes to update nodal velocities and accelerations. In the third step, the nodal data are employed to update the values of accelerations and strain in the MPs. Finally, the assignment of MPs to elements is updated following any mesh adjustments, with the mesh restored to its initial configuration.

Additionally, a specific contact algorithm based on nodal velocities (Ceccato et al., 2017, 2020) was applied to take into account the interactions between the soil and the structure. As plotted in Fig. 2, the procedure of implementing the contact algorithm includes the prediction of nodal velocities based on momentum balance equations and the correction of velocities at the contact nodes i_n, which are calculated before updating the MP information:

$$\left(\boldsymbol{v}_{s,i}^{t+\Delta t}\right)'=\boldsymbol{v}_{s,i}^{t+\Delta t}-\left[\left(\boldsymbol{v}_{s,i}^{t+\Delta t}-\boldsymbol{v}_{s}^{t+\Delta t}\right)\cdot\boldsymbol{n}_i^t\right]\boldsymbol{n}_i^t+\left[\left(\boldsymbol{v}_{s,i}^{t+\Delta t}-\boldsymbol{v}_{s}^{t+\Delta t}\right)\cdot\boldsymbol{n}_i^t\right]\mu\boldsymbol{\tau}_i^t, \tag{3}$$

$$\left(\boldsymbol{v}_{l,i}^{t+\Delta t}\right)'=\boldsymbol{v}_{l,i}^{t+\Delta t}-\left[\left(\boldsymbol{v}_{l,i}^{t+\Delta t}-\boldsymbol{v}_{tl,i}^{t+\Delta t}\right)\cdot\boldsymbol{n}_i^t\right]\boldsymbol{n}_i^t, \tag{4}$$

where $\boldsymbol{v}_{s,i}^{t+\Delta t}$ and $\boldsymbol{v}_{s}^{t+\Delta t}$ are predicted nodal velocities in the solid phase and the system, respectively, $\boldsymbol{v}_{l,i}^{t+\Delta t}$ is the

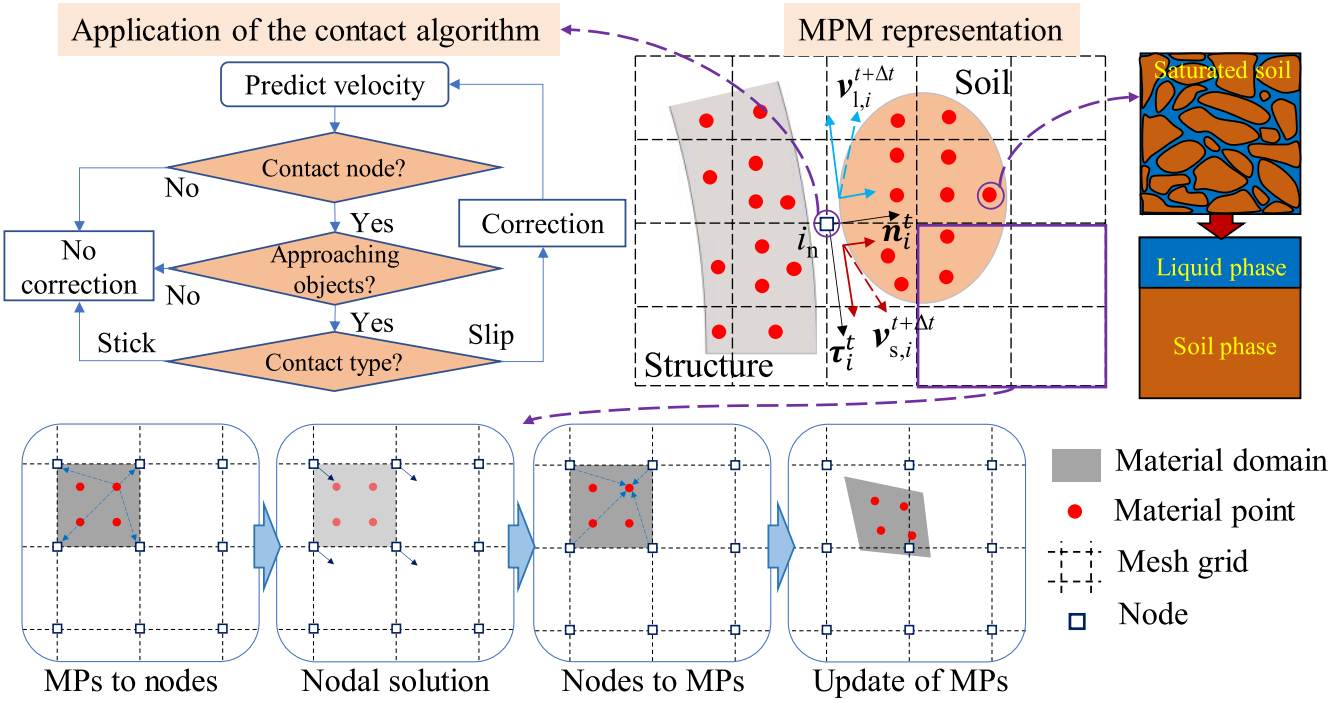

Fig. 2. Schematic of MPM modelling.

predicted nodal velocity for the liquid phase, $\boldsymbol{v}_{\mathrm{l},i}^{t+\Delta t}$ is the nodal velocity for the structure at nodes i_{n}, $\boldsymbol{n}_i^t$ and $\boldsymbol{\tau}_i^t$ are the normal vector and the tangential vector to the soil domain at the node i_{n}, and μ is the coefficient of friction.

The second right-hand term of Eqs. (3) and (4) represents a correction for the normal component to prevent interpenetration. The third term of Eq. (3) accounts for the adjustment of the tangential component to ensure compliance with the contact law. This paper utilizes Anura3D MPM (Anura3D, 2023) to model soil-tunnel interactions. The two-phase MPM formulation is adopted to represent saturated soil behaviour, which follows the Mohr–Coulomb strength criterion.

2.2 FEM modelling of tunnel response

In the MPM framework, the tunnel is modelled as a linear-elastic, homogeneous circular structure, which fails to capture the mechanical behaviour of a tunnel composed of segmental joints, as depicted in Fig. 3(a). Consequently, this study employs an FEM model to simulate the structural response, applying the varying soil and water pressures on the tunnel surface as external loads, which are derived from the MPM modelling.

To accurately calculate the structural forces and deformations of a shield tunnel with segment joints, a data interface must be developed to facilitate the transfer of

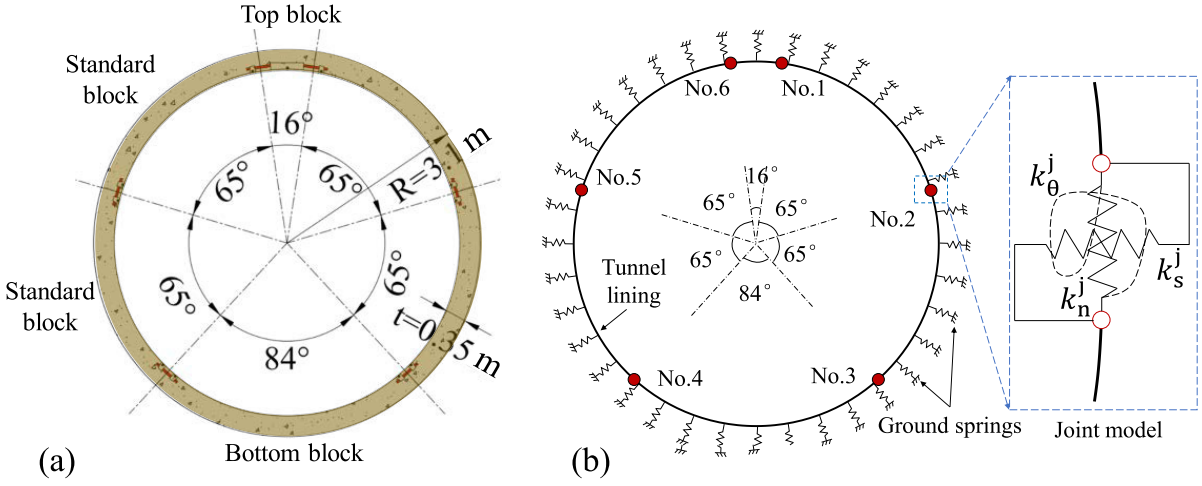

Fig. 3. Schematic of FEM modelling for shield tunnel.

pressures from the MPM model to the FEM model. Application of the contact algorithm allows for the straightforward determination of external pressures acting on the linings after each MPM computation step. Specifically, the nodal forces at the soil-tunnel contact interface can be obtained through the discretized equations:

$$\boldsymbol{f}_{\mathrm{s}} = \int_{\Omega} \boldsymbol{B}^{\mathrm{T}} \boldsymbol{\sigma}_{\mathrm{s}} \mathrm{d}\Omega - \int_{\Omega} (1-n)\rho_{\mathrm{s}} \overline{\boldsymbol{N}}^{\mathrm{T}} \boldsymbol{b} \mathrm{d}\Omega, \tag{5}$$

$$\boldsymbol{f}_{\mathrm{l}} = \int_{\Omega} \boldsymbol{B}^{\mathrm{T}} p_{\mathrm{l}} \boldsymbol{m} \mathrm{d}\Omega - \int_{\Omega} n\rho_{\mathrm{l}} \overline{\boldsymbol{N}}^{\mathrm{T}} \boldsymbol{b} \mathrm{d}\Omega, \tag{6}$$

where $\boldsymbol{f}_{\mathrm{s}}$ and $\boldsymbol{f}_{\mathrm{l}}$ are the vectors of nodal forces over the domain Ω, representing the soil pressure and water pressure on the linings, respectively; σ_{s} denotes the Cauchy stress in the solid phase; $\boldsymbol{B}$ is the strain–displacement matrix; $\overline{\boldsymbol{N}}$ symbolizes the shape function matrix; $\boldsymbol{b}$ indicates the specific body force; $\boldsymbol{m}=(1\ 1\ 1\ 0\ 0\ 0)^{\mathrm{T}}$.

Once the soil and water pressures are derived from the MPM modelling, they can be transferred to the FEM model and applied on the tunnel surface as external loads. Generally, three primary types of FEM models for shield tunnels with segmental joints are commonly employed: the beam-spring model (Zhang et al., 2018), the continuum model with equivalent joints (Wu et al., 2020), and the 3D refined model with detailed joint configurations (Yang et al., 2022; Ye & Liu, 2020, 2021). The beam-spring model is widely utilized for its efficiency in computing deformation and internal forces within linings and joints. The continuum model with equivalent joints is primarily used to assess the effects of joint leakage on both ground and tunnel responses, though it does not account for joint deformation. The 3D model with detailed joint configurations provides an accurate representation of stresses and strains in concrete linings and steel bolts within joints, but it is computationally demanding and often faces convergence issues. In this study, the beam-spring model is employed for FEM modelling due to its ability to facilitate a flexible and efficient data transfer after each MPM calculation step. The data interface and FEM modelling modules were implemented using MATLAB software (MathWorks, 2023). Notably, other FEM models can also be adopted to address the tunnel calculation procedure.

Figure 3(b) presents a schematic diagram of the FEM modelling framework, which primarily comprises the tunnel lining, segmental joints, and soil springs. Furthermore, the lining is represented by beam elements with a stiffness matrix $\boldsymbol{k}_{\mathrm{t}}$. Soil springs ($k_{\mathrm{s}}$) are positioned to incorporate the interaction between the tunnel lining and surrounding soil layers. This study assumes that the direct impact of gushing on soil strength is negligible. Instead, the nonlinear stiffness of soil springs is introduced to realize the effects of gushing-induced tunnel deformation on soil resistance, which is given using the following equation:

$$k_{\mathrm{s}} = \frac{p_{\mathrm{lim}}}{\delta}\left(1 - \frac{p_{\mathrm{lim}}}{p_{\mathrm{lim}} + \eta_0 \delta}\right), \tag{7}$$

where p_{lim} represents the maximal soil reaction forces which can be estimated from the friction angle ϕ and the cohesion values c of the soil (Do et al., 2014); δ is the deformation of soil springs; η_0 is the initial soil stiffness, consisting of the tangential stiffness $\eta_{0,\mathrm{t}}$ and the normal stiffness $\eta_{0,\mathrm{n}}$, which could be defined by Eq. (8):

$$\eta_{0,\mathrm{n}} = \frac{4}{1+\upsilon} \cdot \frac{E}{D}, \tag{8}$$

where D is the tunnel diameter, v represents Poisson's ratio, and E means soil elastic modulus. The normal stiffness is usually assumed to be three times the tangential stiffness (Arnau & Molins, 2011; Plizzari & Tiberti, 2006).

The mechanical properties of the segment joints are modelled using a combination of "axial spring ($k_{\mathrm{n}}^{\mathrm{j}}$) + tangential spring ($k_{\mathrm{s}}^{\mathrm{j}}$) + rotating spring ($k_{\theta}^{\mathrm{j}}$)", which effectively represents the nonlinear behaviour of the joint. Once the element stiffness matrices for both the tunnel lining and segment joints are derived in the global coordinate system, the global stiffness matrix $\boldsymbol{K}_{\mathrm{G}}$ is assembled. External loads $\boldsymbol{P}$ (including soil pressure, water pressure, and gravity) and boundary conditions are applied, and the nodal displacements $\boldsymbol{U}$ are computed using Eq. (9). Based on the nodal displacements, the nodal forces and the relative deformations of elemental nodes in the local coordinate system can be obtained, which are ultimately the internal forces and deformations of the tunnel linings and joints. This type of model for tunnels is also known as a load-structure model.

$$\boldsymbol{K}_{\mathrm{G}} \cdot \boldsymbol{U} = \boldsymbol{P} \Rightarrow \boldsymbol{U} = \boldsymbol{K}_{\mathrm{G}}^{-1} \cdot \boldsymbol{P} \tag{9}$$

2.3 Calculation procedure of MPM–FEM

Figure 4 illustrates the flowchart of the MPM–FEM method. The reliability of the MPM in simulating large soil deformation problems has been validated in prior studies (He et al., 2023), and the performance of the MPM in replicating engineering-scale problems involving water-soil gushing will be further verified through a case study in Section 3. Additionally, the robustness of the FEM model for tunnel analysis has been demonstrated in numerous studies (Yang et al., 2020; Zheng et al., 2016), provided that the applied external loads are appropriate. Therefore, the pressures transferred from the MPM model to the FEM model for application on the tunnel surface must be reasonable, as will be clarified in Section 3. As a result, the MPM–FEM method offers a viable approach for simulating tunnel mechanical behaviour during water-soil gushing.

It is worth noting that the MPM–FEM computational approach is not fully coupled; it involves a unidirectional data transfer from the MPM to the FEM model. Consequently, the structural deformations computed in the FEM model do not feed back to influence the large soil deformations modelled in the MPM. According to the literature (Tan & Lu, 2017; D. Zhang et al., 2019), large soil

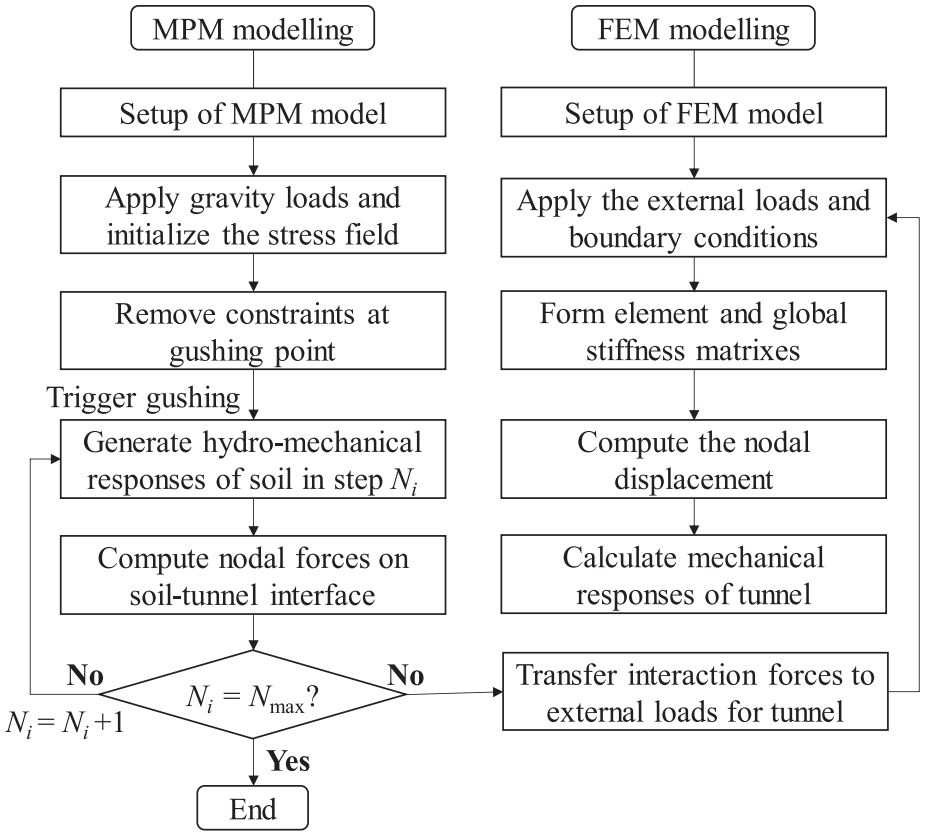

Fig. 4. Framework of water and soil gushing modelling based on MPM–FEM.

deformations in practical cases of water-soil gushing can typically reach several meters, whereas tunnel deformations must be controlled to within a few centimetres. Therefore, it can be inferred that during water-soil gushing, the effect of substantial soil deformation on the tunnel structure is much more significant than the influence of tunnel deformation on the soil. Currently, the development of fully coupled MPM–FEM models for soil-structure interaction is still ongoing (Lei et al., 2022; Wang & Wang, 2023). Thus, the computational method proposed in this paper would be a meaningful exploration for elucidating the large soil deformations and the corresponding structural responses of tunnels caused by gushing. In the future, the development of coupled MPM–FEM models that account for the bidirectional interaction between soil and structure is scheduled for a more comprehensive study of water-soil gushing in tunnels.

3 Water-soil gushing in shield tunnel

3.1 Validation by a case study

Based on the shield tunnelling project in Shanghai, China, a case study was conducted to validate the accuracy and efficiency of the MPM in modelling the gushing in a tunnel. The twin tunnels in this project are horizontally parallel, with an axis spacing of approximately 12.8 m. A detailed cross-sectional diagram is presented in Fig. 5(a). Both tunnels have external diameters of 6.6 m and internal diameters of 5.9 m, giving a lining of 0.35 m thick. The tunnels are situated at an overburden depth of 23.1 m. The tunnels are supposed to pass through a sandy silt layer with high water pressure and high permeability. In this geological condition, improper construction practices pose a significant risk of substantial water inflows carrying sand particles through the segment joints into the tunnels. Unfortunately, an unexpected leakage occurred in the freezing pipes during the construction of the freezing method. Subsequently, large quantities of soil grains quickly gushed into the tunnel through the leakage channel (as shown in Fig. 5) under high water pressure, causing significant tunnel deformation and severe spalling of the tunnel linings. More details are available in the publications (Liu et al., 2020; Zhang et al., 2021).

According to previous studies (Qin et al., 2022; Xie et al., 2022; Zhang et al., 2024), the gushing problems in the twin tunnels could be reduced to a plane strain issue. As shown in Fig. 5(b), the simulation model for gushing is presented, of which the geometric size is 80 m × 50 m. The tunnels are represented using a single-phase elastic material with an elastic modulus of 3.45×10^7 kPa and a Poisson's ratio of 0.2. A two-phase MPM method is employed to simulate the behaviour of the saturated soil, whose parameters are provided in Table 1. The gushing problems are regarded as the drained condition, thus the effective soil parameters are adopted. It should be empha-

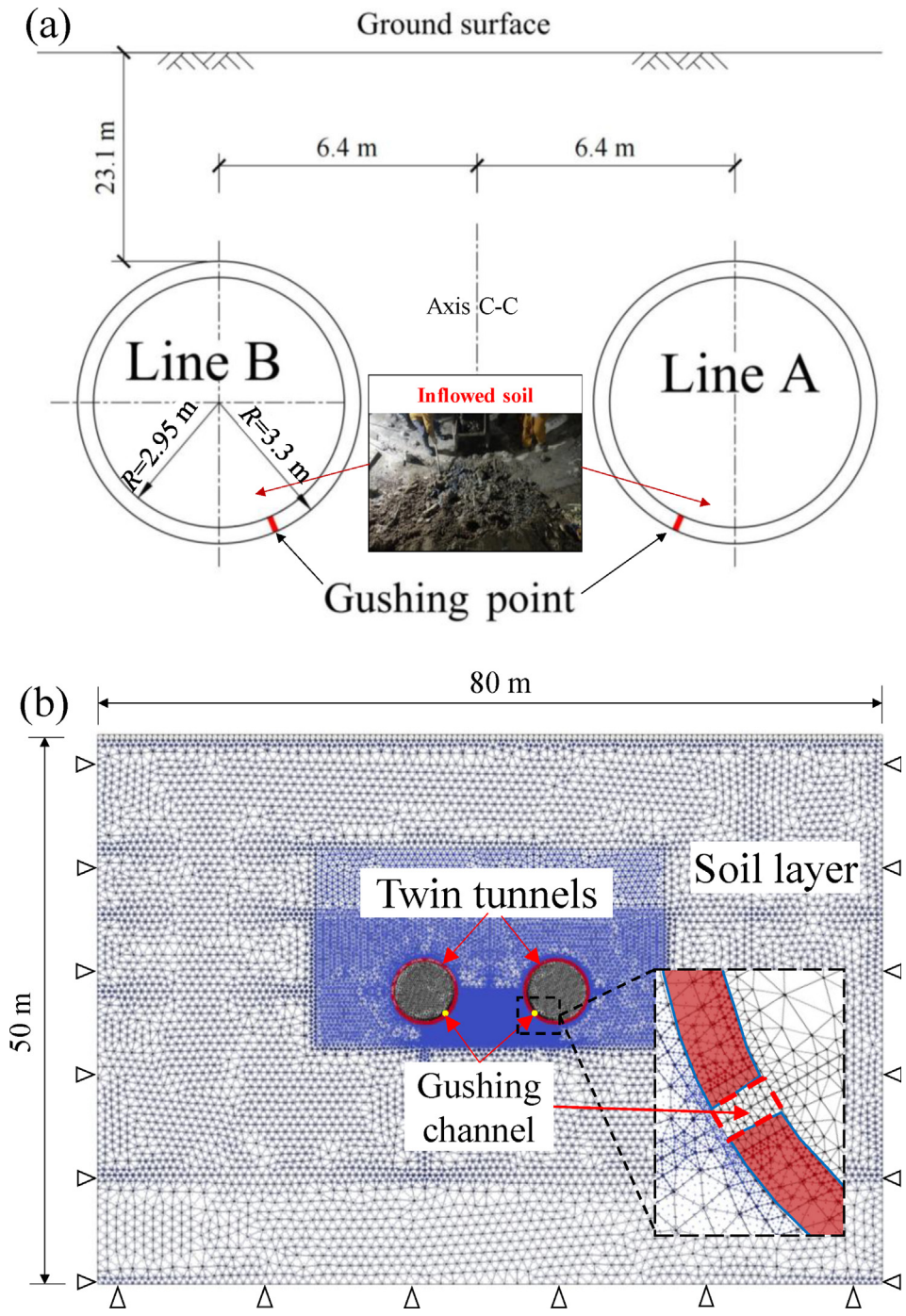

Fig. 5. Geometry of twin tunnels. (a) Cross-section, and (b) simulation model.

sized that in terms of reducing the computational time, the bulk modulus of water was set to be smaller than the physical modulus, which would not substantially affect the numerical results (Martinelli et al., 2017). The above contact algorithm is employed at the soil-tunnel interface to represent the impermeable tunnel with a friction coefficient of 0.2 (Pallett et al., 2002). A 0.2-m wide channel is pre-set to initiate a sudden gushing. The grid consists of triangular elements with a size of 0.75 m, each containing 3 MPs. To enhance computational efficiency without compromising accuracy (Li et al., 2023; Zheng et al., 2023), the element size near the gushing channel in the soil domain is refined to 0.2 m, with 12 MPs per element. As for the boundary constraints for the soil and water phases, the left and right boundaries are fixed horizontally, while the bottom boundary is constrained both horizontally and vertically.

Figure 6 illustrates the ground settlement resulting from the water-soil gushing. Throughout the gushing process,

Table 1
Soil parameters for gushing simulation.

Parameter	Soil type 1	Soil type 2	Soil type 3	Soil type 4	Unit
	Sand	Clay	Sandy silt	Silt	
Cohesion, c	0	5	0	0	kPa
Friction angle, φ	25	25	35	35	(°)
Elastic modulus, E	40 000	40 000	40 000	30 000	kPa
Density of grains, ρ_s	2650				kg/m^3
Poisson ratio, v	0.3				–
Porosity, n	0.45				–
Density of water, ρ_w	1000				kg/m^3
Water bulk modulus, K_w	80 000				kPa
Water viscosity, η_w	1.002×10^{-6}				kPa·s

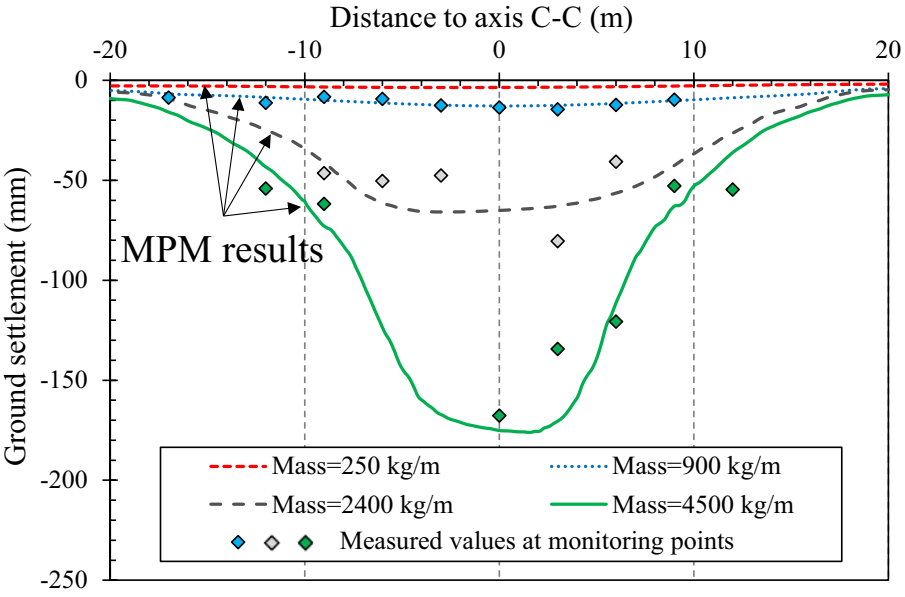

Fig. 6. Ground settlement with different masses of soil inside tunnels.

significant quantities of soil are carried into the tunnel by the seepage flow. The total soil mass entering the tunnel serves as a direct indicator of the progression of the gushing event. To ensure comparability between the numerical results obtained by the MPM and the in-situ measured settlements, the mass of inflowed soil is utilized to represent the state of the gushing. For the numerical simulation, it is the total mass of soils inside the twin tunnels at different stages, demonstrated as lines; for the case study, it is the total mass of soils inside the twin tunnel rings at different monitoring sections, marked as filled points. The monitoring data were obtained from Zhang et al. (2021). It can be seen that the maximal ground settlement increases with the quantity of inflowed soils, but the width of the settlement trough varies less, indicating that the influence range of the gushing on the ground surface mainly stays within 20 m on both sides of the axis C-C (Fig. 5), which is relatively the same as that reflected by the monitoring data. Meanwhile, the calculated ground settlement from the numerical simulation shows good agreement with the measured values at the monitoring points. Therefore, it can be concluded that the MPM approach in this study effectively simulates the large soil deformation process resulting from engineering-scale gushing incidents.

Furthermore, the simulated initial soil pressures on the tunnel surface can be calculated and expanded along the horizontal and vertical directions as shown in Fig. 7. The theoretical values of the initial loads on the tunnel are calculated by the methods in the literature (Zhang et al., 2017). The initial soil pressure distribution acting on the tunnel lining obtained from the MPM modelling matches well with theoretical initial loads before the gushing. The initial distribution of the water pressure is also consistent with a theoretical hydrostatic pressure distribution, which gradually increases along the depth. Thus, the MPM–FEM method can provide reasonable soil and water pressure distributions for analyzing tunnel mechanical behaviours.

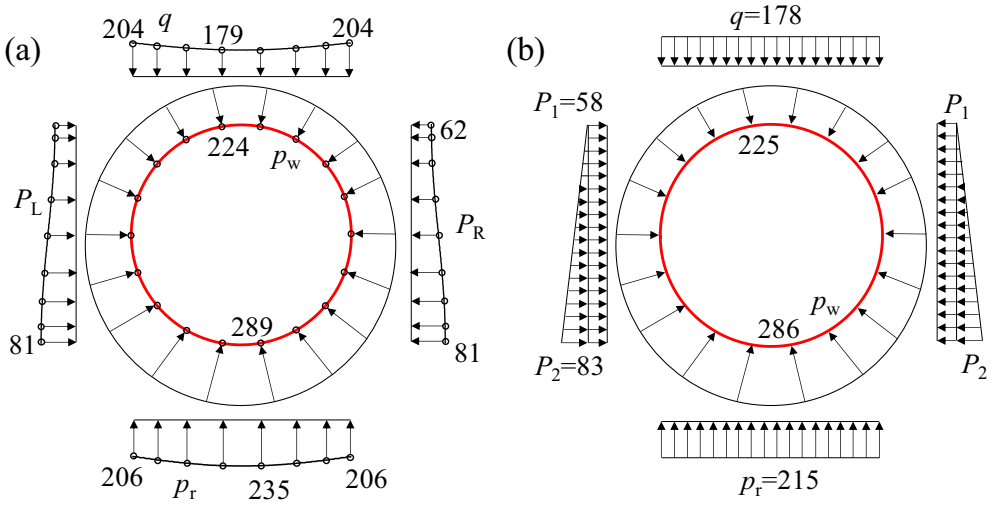

Fig. 7. Comparison of pressures on tunnel. (a) Simulated results, and (b) theoretical results. (Unit: kPa)

3.2 Simulation design for gushing

Based on the aforementioned case study background, this paper analyzes the soil-tunnel response induced by water-soil gushing that occurred in a single tunnel. Figure 8 presents the model setup for the water-soil gushing simulations, with dimensions of 100 m × 50 m. The soil parameters, model boundaries, and other settings were maintained consistently with the case study. In the FEM modelling, the tunnel linings are simulated with beam elements, which are divided into 360 cells. In addition to the geometric configuration being consistent with those in the MPM, the lining segments are also referenced to existing typical metro tunnels. Furthermore, based on the previous studies (Qin et al., 2022; W. Zhang et al., 2020), the following structural parameters are adopted. The segmental joints are modelled with combined springs ($k_\theta^j = 5 \times 10^5$ kN·m/rad/m^2, k_n^j=6 × 10^5 kN/m^3, k_s^j=8 × 10^4 kN/m^3) to reproduce the effects of bolts, and the reaction of soil on the tunnel is simulated with nonlinear soil springs k_s. The loading boundaries of the FEM model are consistent with those of the tunnel in MPM.

The gushing simulation process is divided into three stages: (1) Initially, soil stresses and pore pressures are computed, and restraints are applied at the gushing point to prohibit soil from entering the tunnels. (2) Next, by the removal of these restraints, the soil is allowed to flow into the tunnels within the MPM model. (3) Finally, the soil and water pressure exerted on the lining are calculated and transferred to the FEM model as external loads to determine the internal forces and deformations of the tunnel.

The water and soil gushing process in tunnels is influenced by various factors, including the gushing location, the tunnel depth, and the geological properties. This study conducted a parametric analysis to examine

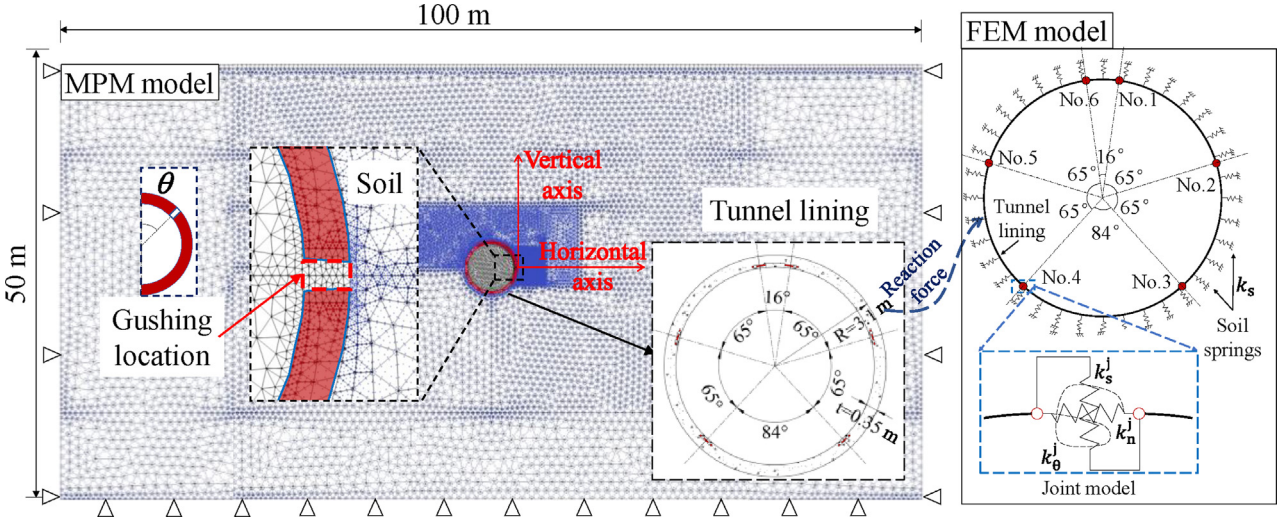

Fig. 8. Model configuration of gushing simulation.

Table 2
Simulation experiment design.

Case number	Gushing location, θ (°)	Soil type	Tunnel depth, H (m)
1	0	1	20
2	45	1	20
3	90	1	20
4	135	1	20
5	180	1	20
6	90	2	20
7	90	3	20
8	90	4	20
9	90	1	5
10	90	1	10

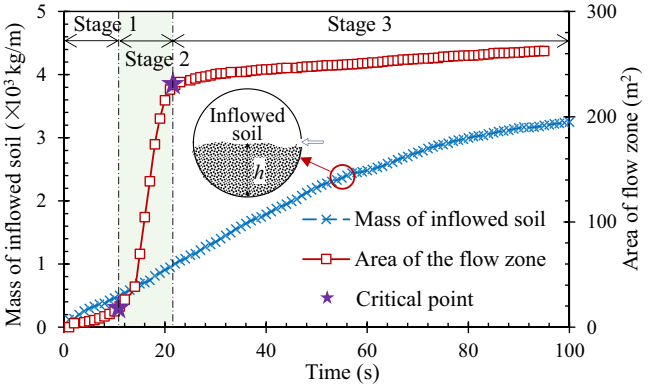

Fig. 9. Development of the gushing process and flow zone.

these influences, focusing on the location of the gushing channel θ (as shown in Fig. 8, representing the angle between the vertical axis and the gushing location), the tunnel buried depth (denoted as H), and the soil properties (including soil elastic modulus E, cohesion c, and friction angle ϕ). Therefore, a total of ten numerical simulations were created, as listed in Table 2. Four distinct soil types, with parameters listed in Table 1, are compared to reveal the influence of the target soil parameter. Except for the variable under investigation, all other conditions remain constant across simulations.

4 Tunnel responses to gushing

According to previous research (Qin et al., 2022; Wang et al., 2014; Ye & Liu, 2020), the leakage occurring in the tunnel waist would have a serious impact on the tunnel structures. So this section firstly emphasizes the case of the gushing location at $\theta = 90°$.

4.1 Development of the hydro-mechanical soil behaviour

Figure 9 shows that the mass of soil rushing into the tunnel was essentially increasing linearly with time. The increasing rate of the inflowed soil mass slightly slowed down after $T = 60$ s, which was mainly due to the height of inflowed soil over the height of the gushing channel, thus affecting the water-soil gushing. It is important to note that an inflowed soil mass of 2000 kg/m represents an extremely dangerous state, far beyond the stage that might be reached in an actual incident (Cheng et al., 2020; D. Zhang et al., 2020; Zhang et al., 2021). Therefore, this study focuses on the results of water-soil gushing before $T = 60$ s to reveal the whole process. In order to properly correlate with the progression of gushing in practical cases, the inflowed soil mass in the tunnel will be used as a reference for the temporal development in the following analysis.

Water-soil gushing causes significant soil deformations surrounding the tunnel, impacting the hydro-mechanical soil behaviour. Figure 10 shows the development of soil hydro-mechanical behaviour when the gushing occurs at location $\theta = 90°$. For a better demonstration, the results of the semi-model are presented here even though the case is not symmetric, because the variations of the soils on the side near the gushing channel are remarkable and distinctive enough to represent the evolution of hydro-mechanical soil behaviour explicitly. As shown in Fig. 10 (a), large soil areas undergo deformation as the gushing progresses, and the affected area gradually stabilises over time. Additionally, there is a smaller region where soil displacement continues to increase consistently.

Based on the characteristics of soil movements, the influenced area in the model could be categorized into three zones: the flow zone (displacement larger than 50 mm), the disturbed zone (displacement varies from 10 to 50 mm), and the stationary zone (displacement smaller than 10 mm). Note that the 50 mm threshold represents the criterion for first-level project impacts on surrounding soils in China (MOHURD, 2014). Figure 10(b) indicates that the shear sliding surface closely aligns with the boundary of the flow zone, which expands progressively from the gushing channel to the ground. This comparison shows that the development of the flow zone could reflect the progression of gushing. Thus, the development of the flow zone is shown in Fig. 9. The whole process could be broken into three stages: (1) the first "initial developing stage", where the flow zone gradually expands; (2) the second "rapid developing stage", where the flow zone area quickly increases; (3) the third "stable developing stage", where the flow zone stabilizes, though soil within the zone continues to rush into the tunnel.

Figure 10(c) and (d) illustrates the development of soil hydro-mechanical responses to the gushing, with flow zone contours included. Within the flow zone, both pore pressure and effective soil stress decrease sharply. In contrast, soil stress increases notably beneath the shear sliding surface, represented by the flow zone contour, especially along the lateral sides of the tunnel. To further elucidate the mechanisms of gushing-induced hydro-mechanical soil behaviours surrounding the tunnel, Fig. 11 displays the patterns of soil stress and pore pressure along the horizontal and vertical axes passing through the gushing point (two axes illustrated in Fig. 8). Overall, both soil stress

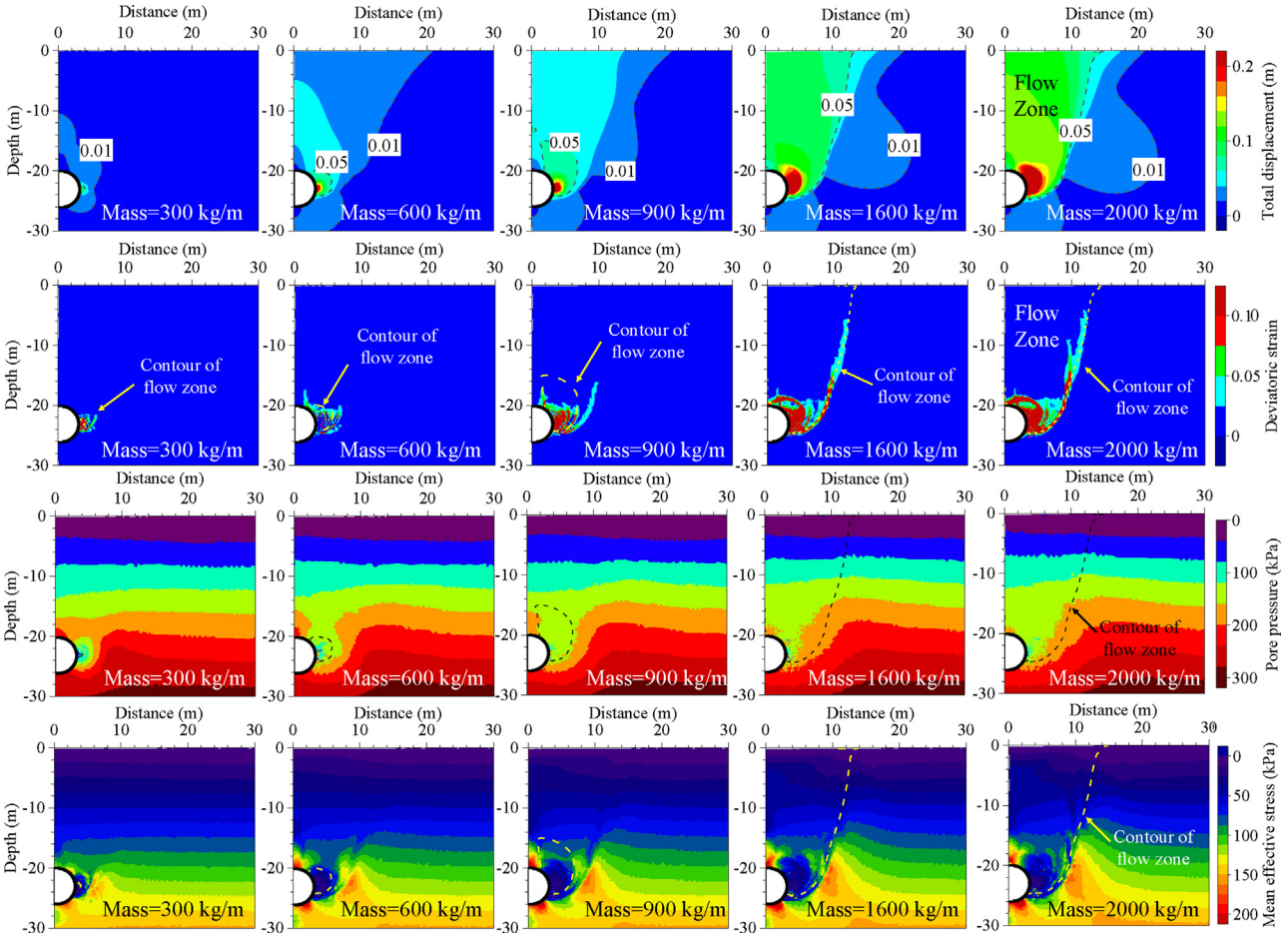

Fig. 10. Evolution of soil behaviours caused by gushing. (a) Soil displacement, (b) deviatoric strain, (c) pore pressure, and (d) effective soil stress.

and pore pressure near the gushing point of the tunnel decrease sharply once the gushing begins. Subsequently, the influence range in the horizontal direction stabilizes at approximately $3D$, where D is the tunnel diameter. The reduction in pore pressure is primarily within a small range of D from the gushing point both in horizontal and vertical directions, giving rise to a significant hydraulic gradient. The decrease in pore pressure around the tunnel led to a redistribution of soil stress. As the horizontal distance from the tunnel increases, soil stress initially increases and then decreases. Meanwhile, soil stress along the vertical axis also shows a local increase at the tunnel top and bottom. Since the soil movement at the tunnel crown and invert was roughly constrained by the tunnel linings, while significant soil deformation occurred in the flow zone due to gushing, a trap-door effect emerged (Pardo & Sáez, 2014; Zheng et al., 2015), leading to the formation of a soil arch around the flow zone.

To describe the soil arch effect, the concept of the stress variation ratio R_σ was introduced (Lee et al., 2006), defined as

$$R_\sigma = \frac{\sigma_t' - \sigma_0'}{\sigma_0'}, \tag{10}$$

where σ_t' is the current effective stress, and σ_0' is the initial effective stress before the gushing starts. Figure 12 shows the distribution of R_σ when the inflowed soil mass reached 2000 kg/m. Positive R_σ, indicating an increase in effective soil stress, is observed at the tunnel crown, tunnel invert, and beneath the sliding surface. Conversely, negative R_σ, representing unloading, appears on the side where gushing occurs. The severe water and soil gushing results in significant unloading of the surrounding soil on the affected side, with effective stress further reduced due to decreased pore pressure. These variations in soil stress and pore pressure around the tunnel, particularly near the gushing points, cause notable changes in the external loads on the tunnel surface, ultimately impacting tunnel structural safety.

4.2 Development of soil and water pressures on lining surface

Throughout the process of gushing, a massive soil mass was carried by the water flow into the tunnel, leading to variations in the soil and water pressure on the lining surface, as displayed in Fig. 13. The distribution of the initial soil pressure varies with the angle θ increasing, and the soil pressure reaches a peak at the tunnel invert ($\theta = 180°$). Since the gushing location is at $\theta = 90°$, the soil pressure

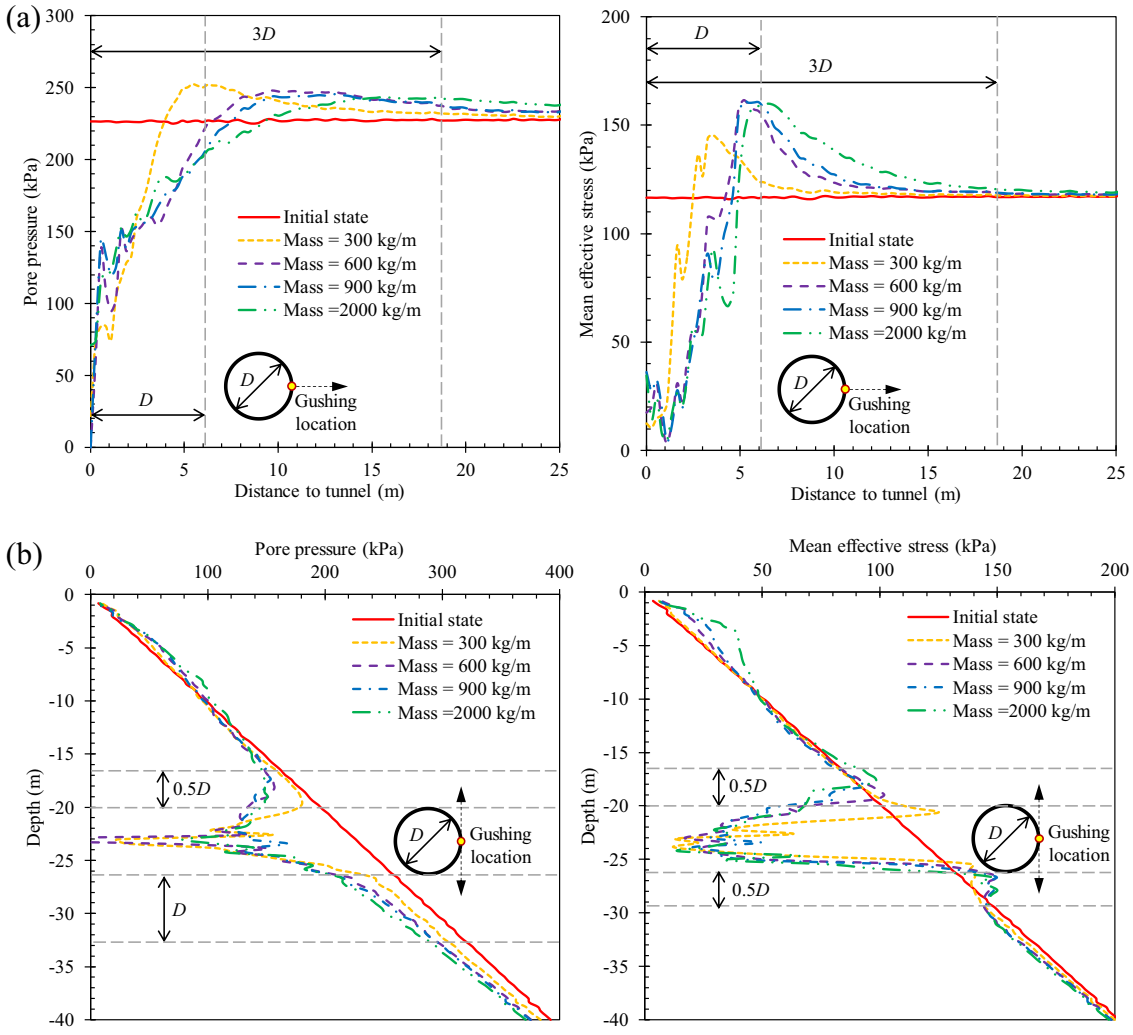

Fig. 11. Development of pore pressure and effective soil stress. (a) Horizontal axis, and (b) vertical axis.

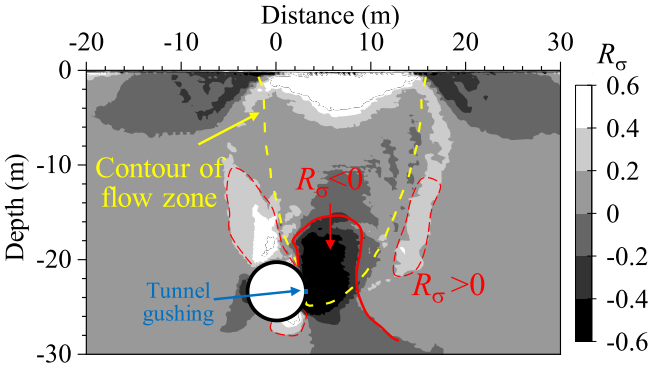

Fig. 12. Soil arching effect induced by water-soil gushing.

around $\theta = 90°$ decreases dramatically due to the gushing, but the soil pressures acting on the tunnel crown and tunnel invert increase. As the gushing progresses, the maximum soil pressure increases by as much as 100% compared to the initial state.

Figure 13(b) shows that the water pressures close to the gushing point ($\theta = 90°$) decrease sharply. The distribution of water pressure stabilizes once the soil inflow mass reaches 1000 kg/m. It is observed that the water pressures on the side nearest to the gushing location are mainly influenced. Furthermore, the impact of gushing on water pressure distribution is generally less extensive than its effect on soil pressure distribution.

To visually demonstrate the evolution of the soil and water pressure on the lining during the gushing, the pressure values are normalized in this study. As shown in Fig. 14, the ratios of the current pressures P_t relative to the initial pressures P_0 are obtained for each stage. After the occurrence of the gushing, the soil and water pressures close to the gushing location are significantly reduced, while the soil pressures near the tunnel crown and tunnel invert increase substantially. With the development of soil loss to 1000 kg/m, the increased rate of the soil pressure near the tunnel invert even reached 100% from the initial state. Such severe variations of the soil and water pressures on the linings will inevitably

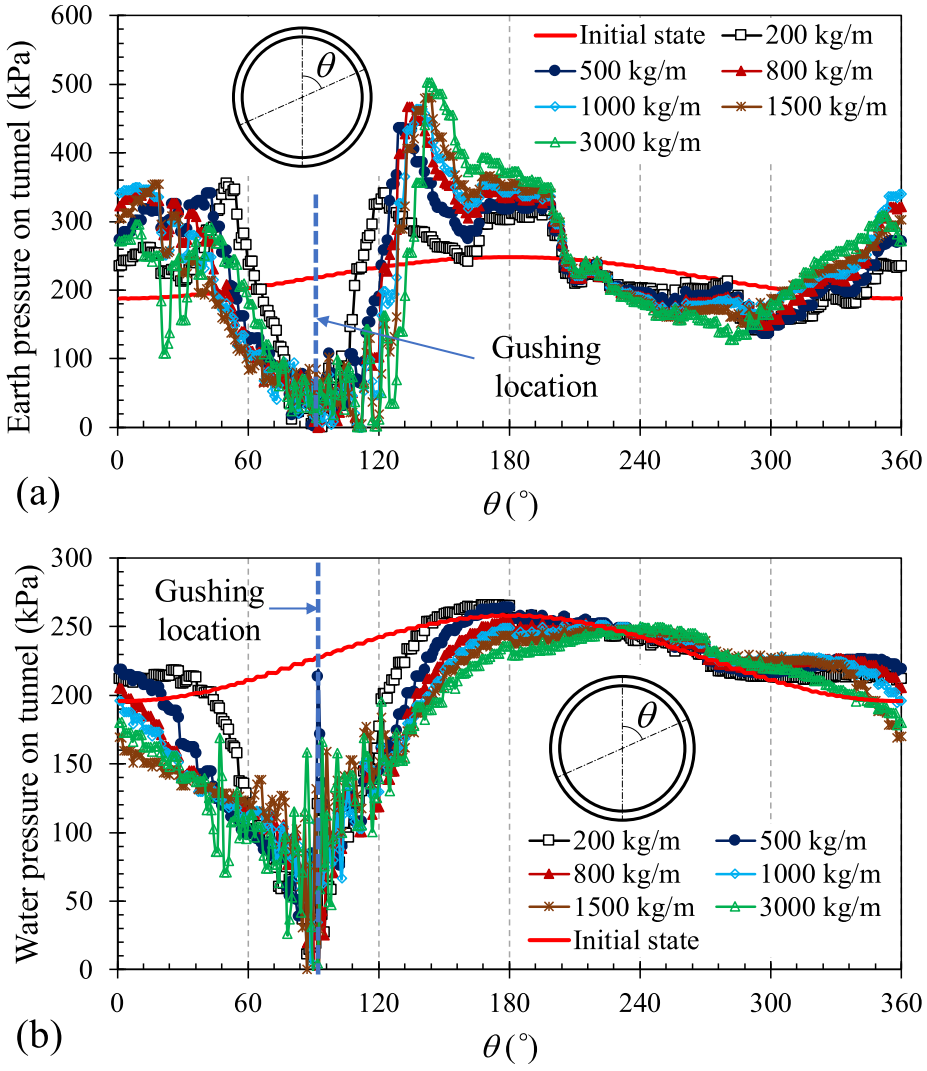

Fig. 13. Development of loads on the lining. (a) Soil pressure, and (b) water pressure.

have a significant impact on the internal force and deformation of the tunnel, which might cause damage to the structures. Therefore, it is of great importance to reveal the development of the responses of tunnel structures under the influence of gushing.

4.3 Progressive mechanical behaviour of tunnel structures

4.3.1 Tunnel linings

Figure 15 illustrates the development of the internal forces of the lining induced by the gushing at a location of $\theta = 90°$. As presented in Fig. 15(a), the axial force of the lining at the tunnel waist is initially the largest. While the impact of gushing on the axial force is minimal, causing only a slight increase near the tunnel waist. Figure 15(b) indicates that the maximal shear forces initially occur at $\theta = 45°$, 135°, 225°, and 315°. Then the maximal shear force increased significantly, with an increase rate reaching up to 114% compared to the initial state. A significant increase in shear force close to a segment joint could lead to intense shear compression between the concrete segments and bolts, potentially resulting in concrete crushing.

Figure 15(c) shows the bending moment distribution before and after the gushing. Positive values represent tension on the outer lining surface, whereas negative ones mean tension on the inner surface. Initially, the outer surface experiences tension within the angles of 45°–135°. The highest positive bending moments are observed at the tunnel waist ($\theta = 90°$). After the gushing, the peak positive bending moment increases by about 82%, while the peak negative bending moment rises by roughly 75%. Overall, the shear forces and the bending moments noticeably increase due to the gushing, particularly on the side adjacent to the gushing location.

Figure 15(d) illustrates the progression of lining deformation resulting from gushing, scaled up by a factor of 100 from the actual values. The following diagrams of the tunnel lining deformation are presented in the same way. As shown in Fig. 15(d), the water-soil gushing can lead to excessive ovalisation of the tunnel because of a

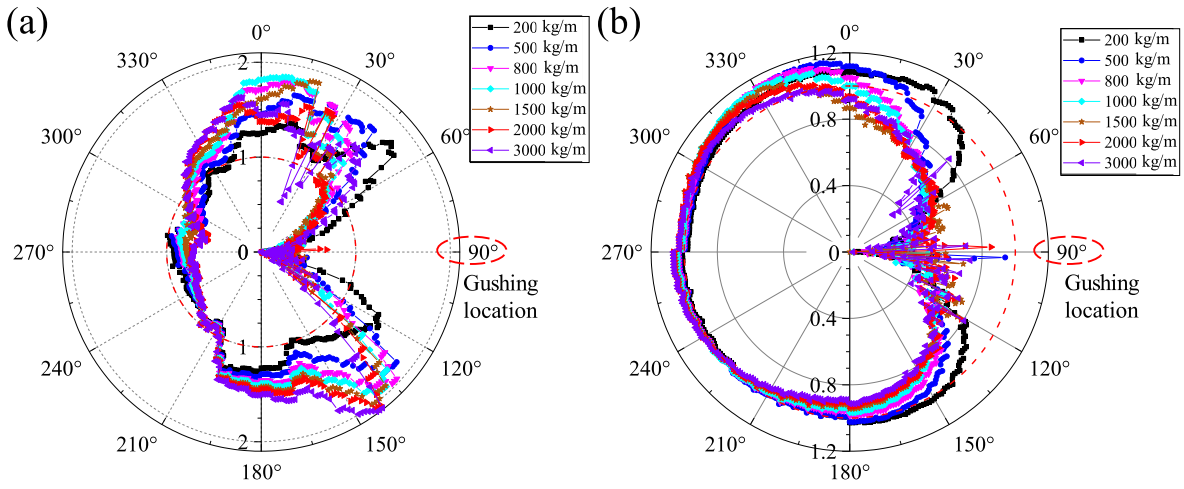

Fig. 14. Development of pressure ratio. (a) Soil pressure, and (b) water pressure.

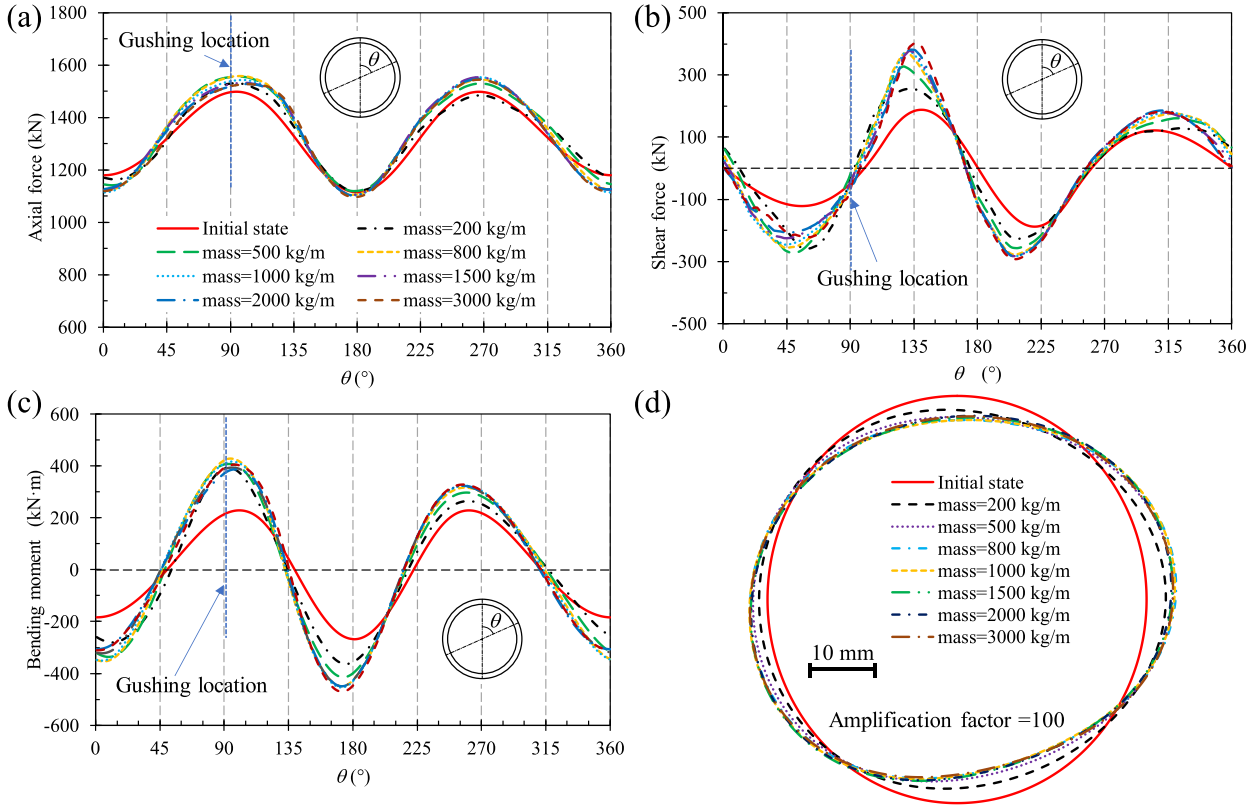

Fig. 15. Development of tunnel mechanical behaviours. (a) Axial force, (b) shear force, (c) bending moment, and (d) lining deformation.

reduction of the soil and water pressure acting on the lining. This could result in a larger opening deformation of the joint and potentially trigger a series of secondary disasters.

To illustrate the impact of water-soil gushing on maximal internal forces, Fig. 16 presents the relationships between the inflowed soil and these internal forces. The locations from which these values were obtained have been discussed in Fig. 15. For instance, the maximal bending moment is located at the tunnel waist, i.e., where the gushing occurs. It is observed that the internal forces in the linings increase sharply following the onset of gushing,

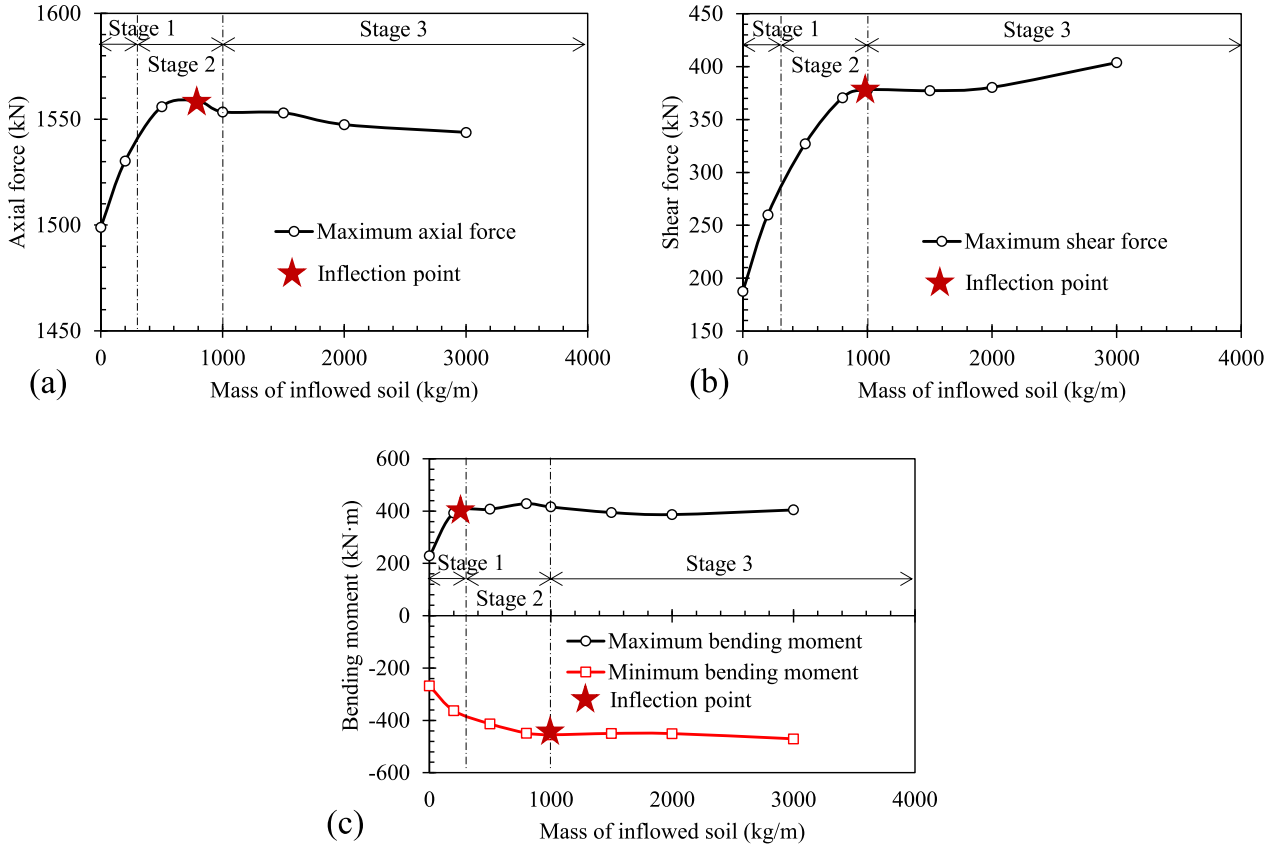

Fig. 16. Development of maximal internal forces. (a) Axial force, (b) shear force, and (c) bending moment.

subsequently stabilizing during the "stable developing stage" (refer to Fig. 9). In summary, the progressive mechanical behaviour of the tunnel is closely linked to the evolution of the flow zone. Notably, the maximal positive bending moment gets to its inflection point faster due to the initial sharp decline in soil and water pressures at this position, where the gushing occurs (see Fig. 13).

4.3.2 Segment joints

As a vital component of shield tunnel structures, the response of segment joints significantly impacts tunnel safety. For instance, excessive deformation of segment joints can lead to waterproofing failure, rendering the tunnel structure hazardous even if the tunnel lining remains intact. Table 3 lists the initial internal forces at the joints, and Fig. 8 shows the location of the joints corresponding to their number. Segment joints primarily bear shear forces within tunnel structures. As indicated in Table 3, the greatest initial shear forces occur at joints No. 3 and No. 4, while the smallest are observed at joints No. 1 and No. 6. As gushing progresses, the internal forces in the segment joints will change, resulting in associated joint deformations, such as openings and dislocations.

Table 3
Initial internal forces of joints.

Joint location	1	2	3	4	5	6
Axial force (kN)	1185	1452	1289	1290	1452	1185
Shear force (kN)	−42	−159	278	−278	159	42
Bending moment (kN·m)	−178	147	3.5	4.5	146	−178

Figure 17 shows the evolution of the joint deformations induced by the gushing. The joint deformations consist of axial, tangential, and rotational components. These values can be directly derived from the relative displacements of the nodal displacements, as mentioned in Section 2.2. Positive values of axial deformation indicate the opening of joints; positive and negative values of shear deformation merely distinguish the direction of dislocation; angular deformation is positive when joints undergo exterior opening and negative for interior opening. These patterns of joint deformation are demonstrated in Fig. 18.

As shown in Fig. 17(a), joints No. 1 and No. 6, along with joint No. 2, show notable axial tensile deformation. In addition, the opening deformations at the joints keep growing until the inflowed soil reaches 1000 kg/m, after which it gradually stabilizes, mirroring the development of lining forces. Figure 17(b) indicates substantial shear deformation in joints No. 1, No. 2, No. 3, and No. 6 following the onset of water-soil gushing, with joint No. 3 continuing to exhibit increasing dislocation. Considering the initially high shear force at joint No. 3, there is a heightened risk of significant longitudinal joint displacement or even concrete spalling.

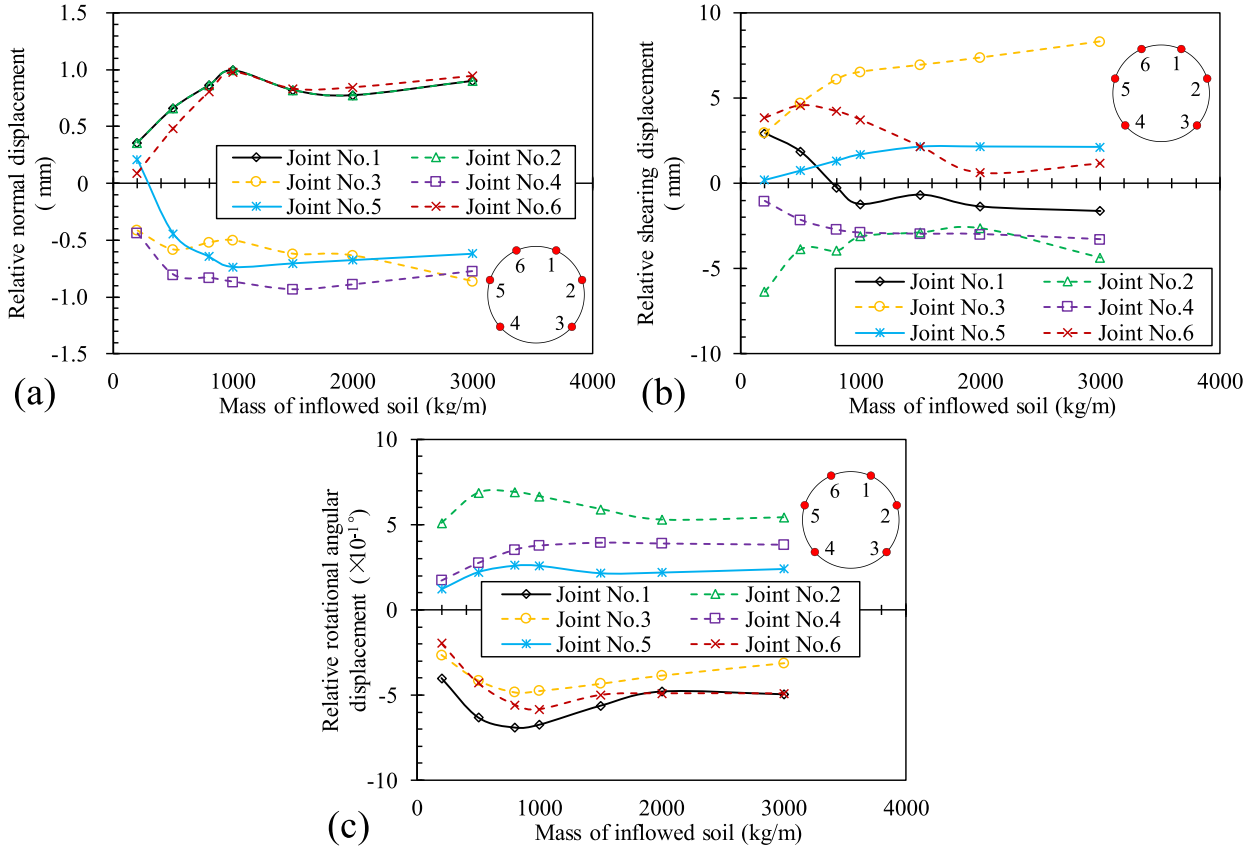

Fig. 17. Development of joint deformation. (a) Axial deformation, (b) shear deformation, and (c) angular deformation.

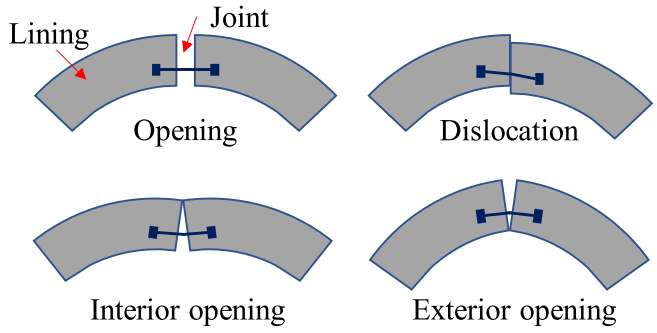

Fig. 18. Deformation pattern of segment joints.

Figure 17(c) reveals notable exterior tensile deformation at joint No. 2, which tends to increase as water-soil gushing progresses. Considering the axial deformation of joint No. 2 presented in Fig. 17(a), it can be concluded that the waterproofing capability of the tunnel is further weakened, which may result in secondary seepage problems and the creation of new pathways for water-soil gushing. Overall, the gushing considerably affects the mechanical properties of joints, which are the weakest parts of the tunnel structures. Therefore, it is crucial to monitor joint deformation and implement protective measures to prevent secondary disasters.

5 Parametric analyses

5.1 Evolution of pressures on tunnel surface

In the process of gushing, a significant soil mass enters the tunnel with the seepage flow, leading to variations in the pressures acting on the linings. To accurately compare the influence of targeted factors rather than the mass of inflowed soil on the tunnel response, the following analyses focus on the stage where the inflow mass is 1000 kg/m. Figure 19 presents the pressure ratio for different gushing locations. The pressure ratio greater than 1 represents that the soil and water pressure increases. As presented in Fig. 19(a), the soil pressure decreases to zero around the gushing location in each case, but the overall distribution of the soil pressure varies. When the gushing point is located in the upper tunnel, the decrease in soil pressure occurs mainly within approximately ± 30° from the gushing location, with minimal impact on the tunnel invert. Conversely, when the gushing location is in the lower half of the tunnel, the soil pressure is affected across the entire tunnel surface, showing an increase in the upper part and a decrease in the lower part. Particularly in the gushing at $\theta = 90°$, the soil pressure at the tunnel invert increases dramatically, with a maximum increase of 100% compared to

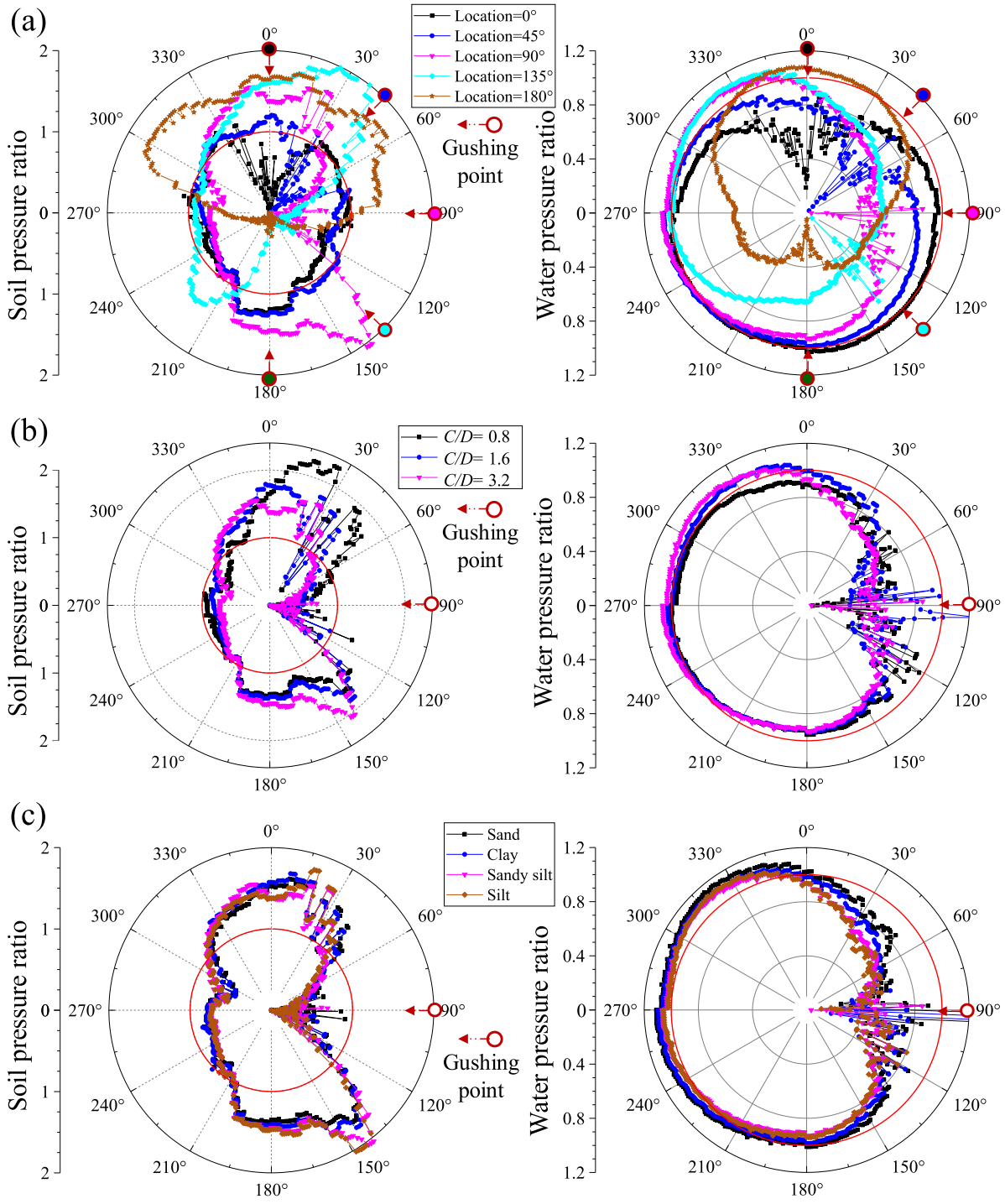

Fig. 19. Comparison of the pressure ratio (for inflowed mass 1000 kg/m). (a) Gushing location, (b) tunnel depth, and (c) soil type.

the initial state. Figure 19(a) also shows the evolution of water pressure acting on the lining in each case. The water pressure decreases to zero around the gushing location. It can be observed that the extent of water pressure reduction gradually increases as the gushing location descends. For example, in the gushing at $\theta = 0°$, the water pressure is affected in the upper part of the tunnel, while in the gushing at $\theta = 180°$, the influence range is from $\theta = 30°$ to 330°. In conclusion, the lower the gushing location, the greater the influence of gushing on the tunnel.

Figure 19(b) illustrates the pressure ratios on the tunnel surface at varying tunnel depths. To facilitate visual comparisons between different tunnel scenarios, the cover-to-diameter ratio (C/D), which is the ratio of the overburden depth to the diameter of the tunnel, is used to represent the effect of tunnel depth in the following analysis. Despite the

differences in the tunnel depth, the distribution patterns of soil and water pressures due to the gushing remain consistent. However, the soil pressure ratio at the tunnel invert increases with greater tunnel depth. It is vital to note that the initial soil and water pressures vary for different tunnel depths, leading to different absolute reductions in soil and water pressures for each case. Figure 19(c) presents the pressure ratios of the soil and water pressure for different soil types. Comparing the results for sand and clay indicates that the cohesion of the soil layer has a minimal influence on the overall distribution of soil and water pressure. In contrast, comparing soil types of sand and sandy silt reveals that an increase in friction angle exacerbates the variation in soil and water pressures. A comparison of sandy silt and silt demonstrates that the elastic modulus has little impact on the evolution of the soil and water pressures acting on the lining surface.

5.2 Mechanical responses of tunnel lining

Figure 20 compares the distributions of the additional internal forces due to the gushing with the same amount of soil inflow. It can be observed from Fig. 20(a) that the additional axial forces and bending moments vary noticeably for different gushing locations. In each case, the internal forces at the gushing point usually increase sharply due to the gushing. As the gushing location descends, the additional bending moment gradually increases. For example, in the cases of the gushing location at $\theta = 90°$ and $\theta = 135°$, the bending moment at the tunnel invert increased by 80% from the initial value (–267 kN·m). In the gushing at $\theta = 180°$, the additional bending moment is smaller than in the cases above. This is because the distribution of surface pressures on the lining is symmetric along the vertical axis of the tunnel when the gushing location is at $\theta = 180°$ (Fig. 19), and the variations in surface pressure primarily result in overall tunnel settlements rather than increasing tunnel deflection. After all, the additional axial forces are sufficiently small compared to the initial axial forces (1115–1499 kN).

Figure 20(b) shows that, although the tunnel depth in each case is different, the distributions of the additional axial forces and bending moments induced by the gushing are consistent. The maximum internal forces in all cases are increasing, thus exacerbating the risk to the tunnel lining. Furthermore, the deeper the tunnel is buried, the greater the variation in internal forces induced by the same mass of inflowed soil. Figure 20(c) presents the effects of soil types on the additional internal forces caused by the gushing. Comparing soil types of sandy silt and silt indicates that the variation in soil modulus has nearly no effect on the internal forces of the tunnel. The results of sand and clay show that the increase of the cohesion will slightly increase the variation of the internal force. In addition, a comparison of sand and sandy silt indicates that a reduction of the friction angle can give rise to a decrease in the internal forces, which corresponds to the influence of the friction angle on the soil and water pressures due to the gushing.

The evolution of the lining deformation and the internal forces is related, and together they demonstrate the mechanical response law of the tunnel structure during the process of gushing. Figures 21 and 22 show the deformation of the tunnel when the soil inflow mass is 1000 kg/m in different cases. As presented in Fig. 21(a), the tunnel deformations in the gushing at $\theta = 90°$ and $\theta = 135°$ are significant. The tunnel lining in the gushing at $\theta = 135°$ even undergoes asymmetrical deformation, while the corresponding tunnel convergence is rather small, as depicted in Fig. 22(a). Due to the decrease in surface pressures at the gushing point (Fig. 19), the tunnel exhibits increasingly pronounced settlement as the gushing location descends. It can be concluded that the gushing point in the lower tunnel has the most drastic influence on the mechanical responses of the lining. The gushing at $\theta = 90°$ is the most representative, in which the additional bending moments and the lining deformations due to the water-soil gushing are the most significant, as well as the tunnel convergence.

Figures 21(b) and 22(b) show the tunnel deformations when the soil inflow mass is 1000 kg/m for different tunnel depths. Similar to the distribution law of the internal force induced by the gushing, the development pattern of the tunnel deformation is hardly affected by the tunnel depth, except for the maximum deformation. The linings are subject to "horizontal expansion" deformation, which increases with tunnel depth. The tunnel convergence and vertical settlement in the case of $C/D = 3.2$ are approximately 7.4 times and 13.9 times those in the case of $C/D = 0.8$, respectively. In conclusion, in the case of a larger tunnel depth, the gushing will cause a more severe effect on the responses of the linings.

Figures 21(c) and 22(c) compare the gushing-induced lining deformation in cases of different soil types. According to the comparison of sandy silt and silt, the elastic modulus shows little effect on the development of the tunnel deformation, in parallel with the impact of the soil types on the internal forces. Soil types with higher cohesion and friction angle would slightly increase the gushing-induced tunnel deformation and convergence. With the evolution of the internal forces and deformations of the tunnel lining in different soil types, it can be deduced that the greater soil shear strength does not represent a lower risk of gushing-induced damage to the structure. On the contrary, after the surrounding soil undergoes large deformation due to gushing in the tunnel, the internal forces and deformations of the tunnel lining in the soil layer with higher shear strength will be greater.

5.3 Deformation of segment joints

Figure 23 compares the gushing-induced deformation of the segment joints in different cases. The horizontal axis represents the location of the joint in each case. As shown

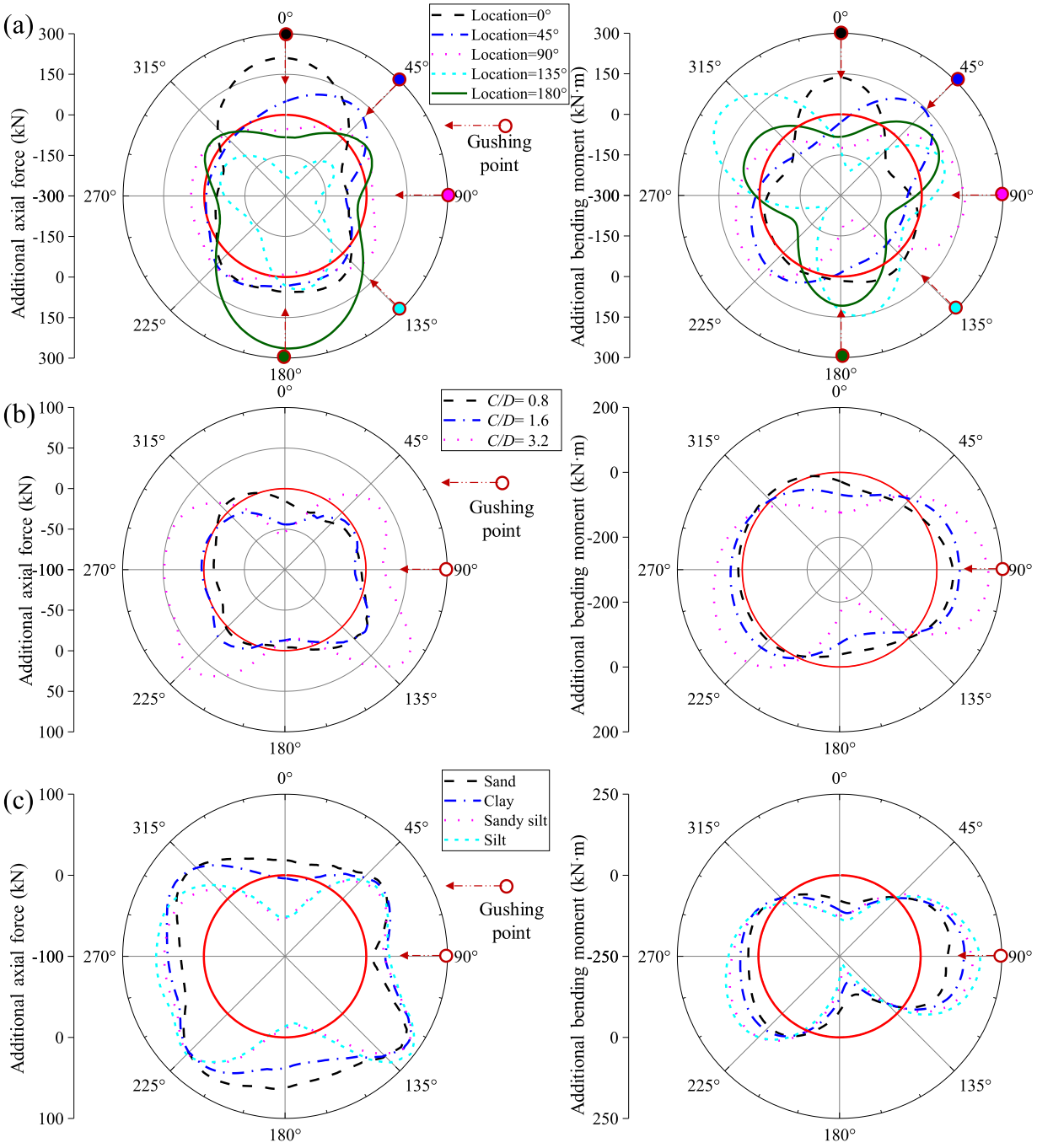

Fig. 20. Gushing-induced additional internal forces in different cases. (a) Gushing location, (b) tunnel depth, and (c) soil type.

in Fig. 23(a), the opening deformations of the joint in the case of gushing location $\theta = 90°$ and $\theta = 135°$ are the largest. The dislocations are also generated, and the most significant dislocations are observed in the cases of gushing locations $\theta = 90°$ and $\theta = 180°$. These joint deformations will affect the waterproofing of the tunnel and even the structural strength. Therefore, it can be considered that if the gushing point is at the lower part of the tunnel, the joints will be in a more dangerous state under the influence of the gushing, which is inextricably linked to the significant development of mechanical responses of the tunnel.

Figure 23(b) compares the effects of different tunnel depths on the deformation of segment joints induced by gushing. It can be observed that the increase in tunnel depth essentially does not change the deformation characteristics of the joint in all cases, but only enlarges the joint deformations. For instance, joints No. 2 and No. 5 exhibit an external opening deformation in all cases. With certainty, the

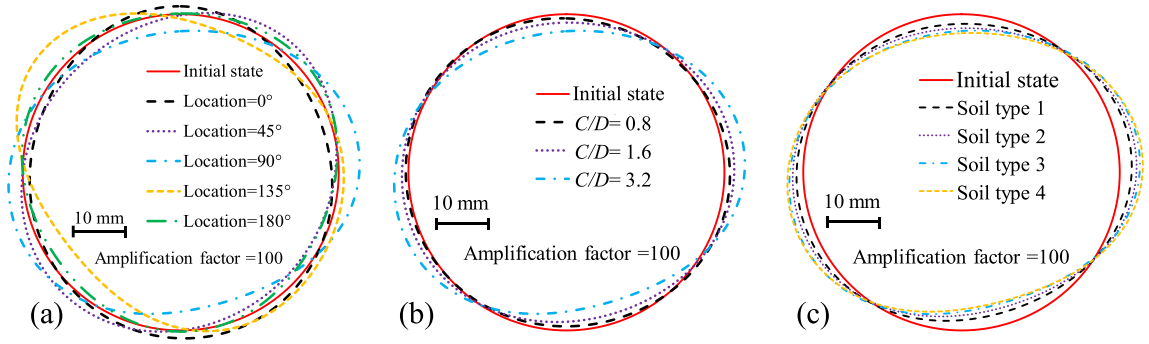

Fig. 21. Effect of different factors on the lining deformation. (a) Gushing location, (b) tunnel depth, and (c) soil type.

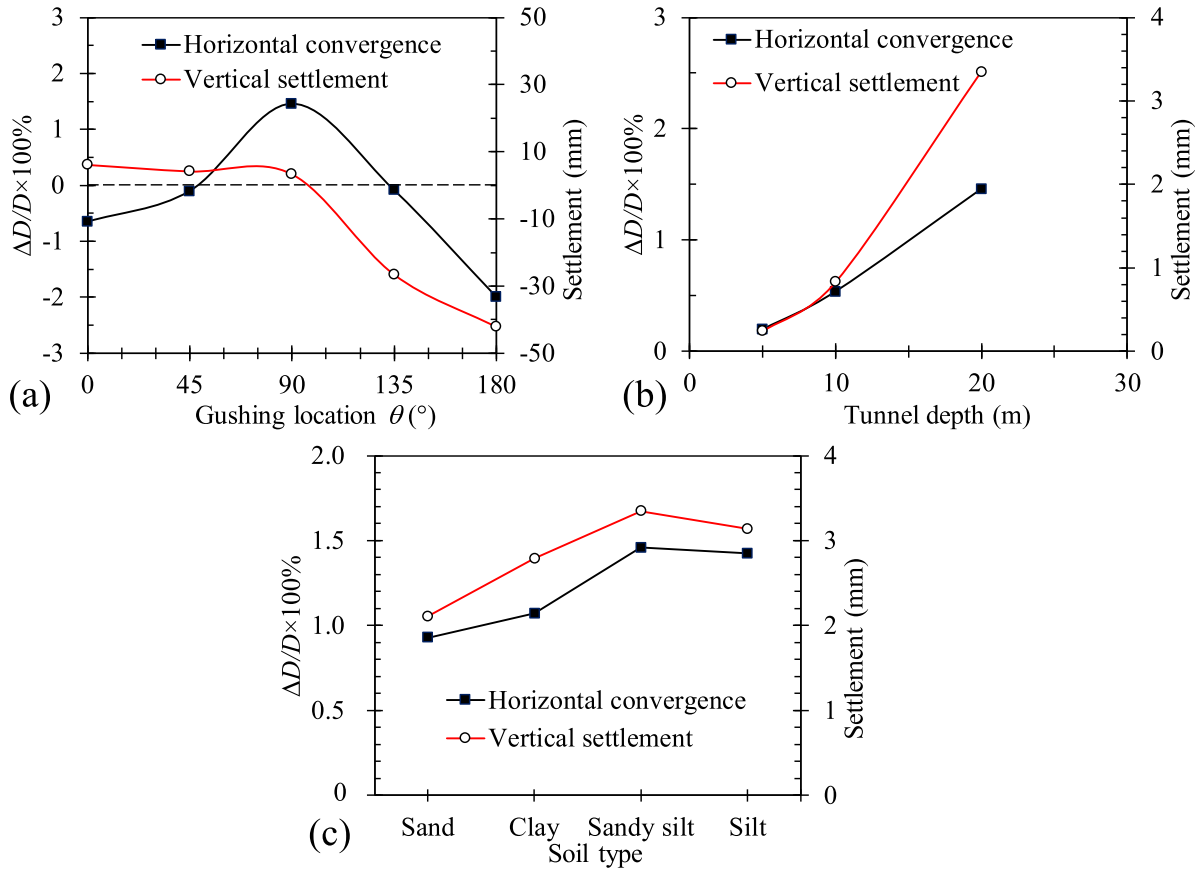

Fig. 22. Development of tunnel displacement in different cases. (a) Gushing location, (b) tunnel depth, and (c) soil type.

increased tunnel depth will place the joints that are under the influence of the gushing in a more endangered state. Therefore, the greater the tunnel depths are, the greater the impact of the gushing on the tunnel structures.

Figure 23(c) presents the joint deformations due to the gushing in the cases of different soil types. Since the elastic modulus has nearly no effect on the soil and water pressures on the lining surface, its effect on joint deformation can also be neglected. By comparing the results for sand and sandy silt, the increase in friction angle significantly amplifies the opening deformations of joints No. 1, 2, 5, and 6, which are located in the upper part of the tunnel. Meanwhile, the dislocations of joints No. 3 and 4 also increase as the friction angle rises. All in all, when the soil shear strength increases, the gushing-induced joint deformation increases. Therefore, enhancing water resistance is more effective in mitigating the severe consequences of gushing than reinforcing the surrounding soil.

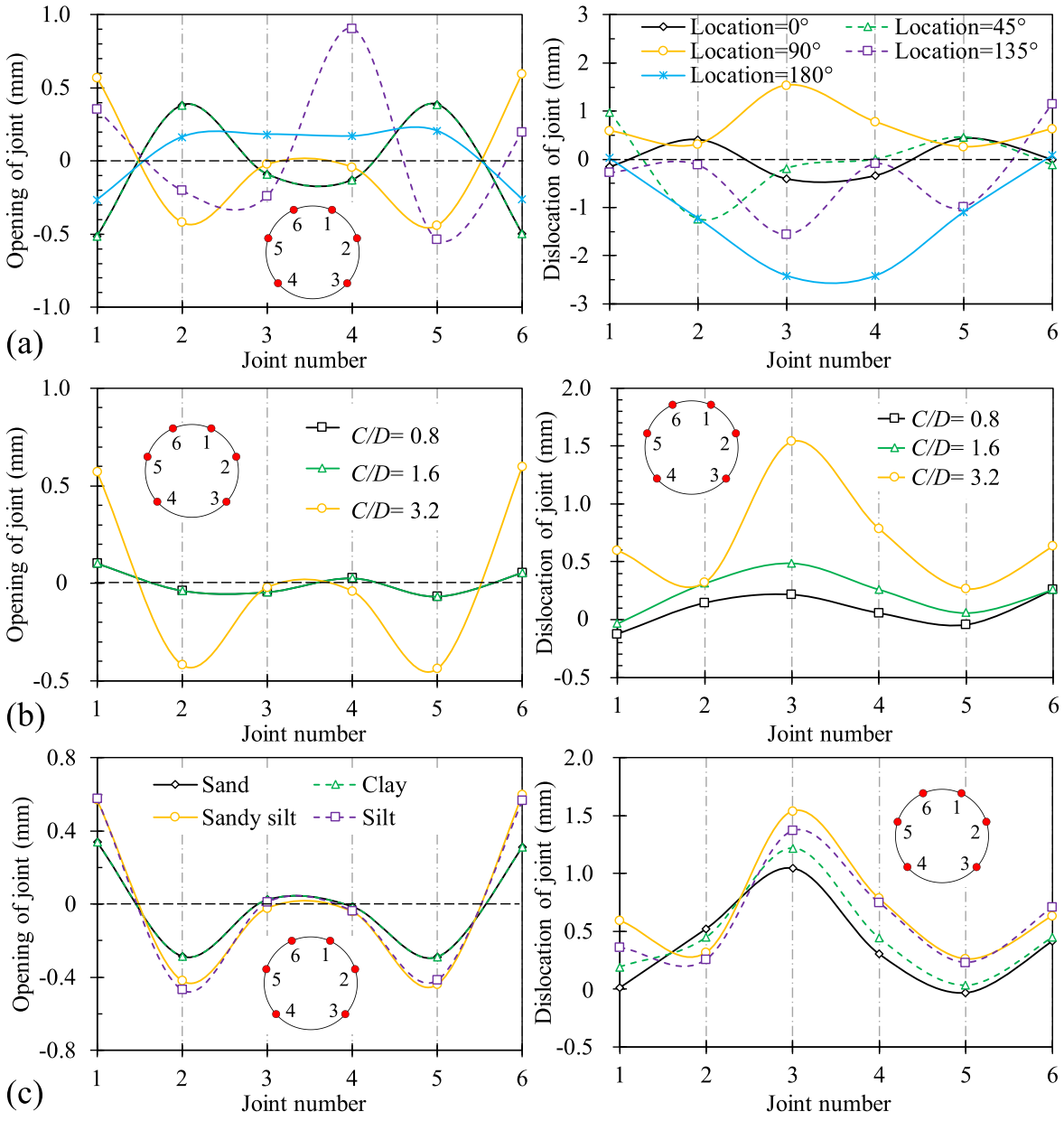

Fig. 23. Effect of different factors on joint deformations. (a) Gushing location, (b) tunnel depth, and (c) soil type.

6 Conclusions

This study has carried out an in-depth study on the evolution of the tunnel mechanical responses caused by gushing. Firstly, based on the MPM–FEM approach, a framework of water-soil gushing modelling was established. Then, a case study was carried out, and the development of the structural internal forces and deformations was revealed. Finally, the effects of gushing location, tunnel depths, and soil types on the mechanical behaviours of the structures owing to the gushing were investigated. The main findings can be listed as follows:

(1) The framework of water-soil gushing modelling based on the MPM–FEM approach is proven to accurately simulate gushing-induced large soil deformations and the associated mechanical behaviours of the tunnels with joints, which is vital for understanding and mitigating the impacts of gushing on underground infrastructures.

(2) The hydro-mechanical behaviour of the soil surrounding the tunnel is significantly influenced, which can be defined as the flow zone, disturbed zone, and stationary zone. The affected range of pore pressure and soil stress by the gushing is approximately within three times the

diameter from the point of gushing. Furthermore, a soil arch developed around the flow zone at a distance of one tunnel diameter from the gushing point.

(3) The mechanical response of tunnel structures to water-soil gushing is characterized by significant changes in internal forces and deformation patterns. This study revealed that shear forces and bending moments in the tunnel lining undergo notable variations, with maximum increments of 114% and 82%, respectively, which could lead to severe structural diseases such as joint opening, segment dislocation, and waterproofing failures, particularly at weak joints No. 2 and No. 3.

(4) The lower the gushing location, the more significant the change in the internal forces of linings. The gushing at $\theta = 90°$ and $\theta = 135°$ causes bending moments to increase by 80% from the initial value. Additionally, deeper tunnel depths exacerbate these mechanical responses of tunnels, and the tunnel settlement in the case of $C/D = 3.2$ is approximately 13.9 times that in the case of $C/D = 0.8$. Furthermore, the gushing-induced additional internal forces and deformations of the tunnel will be greater in the soil layer with higher shear strength.

(5) The joint deformation caused by the gushing is also influenced by gushing location, tunnel depth, and soil properties. As the gushing point moves downward, the joint deformations, including joint opening and dislocations, increase significantly. In addition, the deeper the tunnel, the greater the impact of gushing on the joints. Moreover, gushing in soil layers with higher shear strength leads to larger opening deformations of joints located in the upper part of the tunnel.

Data availability

The data that support the findings of this study are available from the corresponding author upon reasonable request.

CRediT authorship contribution statement

Xiao-Chuang Xie: Writing – original draft, Validation, Data curation, Writing – review & editing, Visualization, Conceptualization, Software. **Dong-Mei Zhang:** Writing – review & editing, Supervision, Conceptualization. **Ming-Liang Zhou:** Supervision, Software, Writing – review & editing.

Declaration of competing interest

The authors declare that they have no known competing financial interests or personal relationships that could have appeared to influence the work reported in this paper.

Acknowledgement

This work was financially supported by the Key Research and Development Program of China (Grant No. 2023YFC3009302), National Natural Science Foundation of China (Grant Nos. 52238010, 52408436, 52090082, and 52108381), Shanghai Pujiang Programme (23PJD104), Innovation Program of Shanghai Municipal Education Commission (Grant No. 2019-01-07-00-07-456 E00051), and Shanghai Science and Technology Committee Program (Grant Nos. 22XD1430200, 21DZ1200601, and 20DZ1201404).

References

Anura3D. (2023). *Anura3D MPM software v. 2023*.

Arnau, O., & Molins, C. (2011). Experimental and analytical study of the structural response of segmental tunnel linings based on an in situ loading test. *Tunnelling and Underground Space Technology, 26*(6), 764–777.

Bandara, S., & Soga, K. (2015). Coupling of soil deformation and pore fluid flow using material point method. *Computers and Geotechnics, 63*, 199–214.

Bardenhagen, S. G., Guilkey, J. E., Roessig, K. M., Brackbill, J. U., Witzel, W. M., & Foster, J. C. (2001). An improved contact algorithm for the material point method and application to stress propagation in granular material. *Computer Modeling in Engineering and Sciences, 2*(4), 509–522.

Ceccato, F., Beuth, L., & Simonini, P. (2017). Adhesive contact algorithm for MPM and its application to the simulation of cone penetration in clay. *Procedia Engineering, 175*, 182–188.

Ceccato, F., Beuth, L., Vermeer, P. A., & Simonini, P. (2016). Two-phase material point method applied to the study of cone penetration. *Computers and Geotechnics, 80*, 440–452.

Ceccato, F., Bisson, A., & Cola, S. (2020). Large displacement numerical study of 3D plate anchors. *European Journal of Environmental and Civil Engineering, 24*(4), 520–538.

Ceccato, F., Yerro, A., & Di Carluccio, G. (2024). Simulating landslides with the material point method: Best practices, potentialities, and challenges. *Engineering Geology, 338*, 107614.

Ceccato, F., Yerro, A., Girardi, V., & Simonini, P. (2021). Two-phase dynamic MPM formulation for unsaturated soil. *Computers and Geotechnics, 129*, 103876.

Chen, Z. P., Qiu, X. M., Zhang, X., & Lian, Y. P. (2015). Improved coupling of finite element method with material point method based on a particle-to-surface contact algorithm. *Computer Methods in Applied Mechanics and Engineering, 293*, 1–19.

Cheng, W. C., Li, G., Liu, N., Xu, J., & Horpibulsuk, S. (2020). Recent massive incidents for subway construction in soft alluvial deposits of Taiwan: A review. *Tunnelling and Underground Space Technology, 96*, 103178.

Do, N. A., Dias, D., Oreste, P., & Djeran-Maigre, I. (2014). A new numerical approach to the hyperstatic reaction method for segmental tunnel linings. *International Journal for Numerical and Analytical Methods in Geomechanics, 38*(15), 1617–1632.

Fern, E. J. (2019). Modelling tunnel-induced deformations with the material point method. *Computers and Geotechnics, 111*, 202–208.

Fern, J., Rohe, A., Soga, K., & Alonso, E. (2019). *The material point method for geotechnical engineering*. CRC Press.

He, K., Xi, C. J., Liu, B., Hu, X. W., Luo, G., Ma, G. T., & Zhou, R. C. (2023). MPM-based mechanism and runout analysis of a compound reactivated landslide. *Computers and Geotechnics, 159*, 105455.

Huang, L. C., Ma, J. J., Lei, M. F., Liu, L. H., Lin, Y. X., & Zhang, Z. Y. (2020). Soil-water inrush induced shield tunnel lining damage and its stabilization: A case study. *Tunnelling and Underground Space Technology, 97*, 103290.

Jassim, I., Stolle, D., & Vermeer, P. (2013). Two-phase dynamic analysis by material point method. *International Journal for Numerical and Analytical Methods in Geomechanics, 37*(15), 2502–2522.

Kafaji, I. K. J. (2013). *Formulation of a Dynamic Material Point Method (MPM) for Geomechanical Problems* [Doctoral dissertation, University of Stuttgart, Germany].

Lee, C. J., Wu, B. R., Chen, H. T., & Chiang, K. H. (2006). Tunnel stability and arching effects during tunneling in soft clayey soil. *Tunnelling and Underground Space Technology, 21*(2), 119–132.

Lei, Z. D., Wu, B. S., Wu, S. S., Nie, Y. X., Cheng, S. Y., & Zhang, C. Y. (2022). A material point-finite element (MPM-FEM) model for simulating three-dimensional soil-structure interactions with the hybrid contact method. *Computers and Geotechnics, 152*, 105009.

Li, J. G., Wang, B., Wang, D., Zhang, P., & Vardon, P. J. (2023). A coupled MPM-DEM method for modelling soil-rock mixtures. *Computers and Geotechnics, 160*, 105508.

Lian, Y. P., Zhang, X., & Liu, Y. (2011). Coupling of finite element method with material point method by local multi-mesh contact method. *Computer Methods in Applied Mechanics and Engineering, 200* (47–48), 3482–3494.

Lin, W., Li, P., & Xie, X. Y. (2022). A novel detection and assessment method for operational defects of pipe jacking tunnel based on 3D longitudinal deformation curve: A case study. *Sensors, 22*(19), 7648.

Lin, W., Li, P., Xie, X. Y., Cao, Y. Y., & Zhang, Y. B. (2023). A Novel back-analysis approach for the external loads on shield tunnel lining in service based on monitored deformation. *Structural Control and Health Monitoring, 2023*, 8128701.

Lin, W., Sheil, B., Zhang, P., Zhou, B., Wang, C., & Xie, X. Y. (2024). Seg2Tunnel: A hierarchical point cloud dataset and benchmarks for segmentation of segmental tunnel linings. *Tunnelling and Underground Space Technology, 147*, 105735.

Liu, D. J., Wang, F., Hu, Q. F., Huang, H. W., Zuo, J. P., Tian, C., & Zhang, D. M. (2020). Structural responses and treatments of shield tunnel due to leakage: A case study. *Tunnelling and Underground Space Technology, 103*, 103471.

Long, Y. Y., & Tan, Y. (2020). Soil arching due to leaking of tunnel buried in water-rich sand. *Tunnelling and Underground Space Technology, 95*, 103158.

Lu, M., Ceccato, F., Zhou, M. L., Yerro, A., & Zhang, J. (2024). Evaluating the exceedance probability of the runout distance of rainfall-induced landslides using a two-stage FEM-MPM approach. *Acta Geotechnica, 19*, 3691–3706.

Ma, J., Wang, D., & Randolph, M. F. (2014). A new contact algorithm in the material point method for geotechnical simulations. *International Journal for Numerical and Analytical Methods in Geomechanics, 38*(11), 1197–1210.

Mair, R. J. (2008). Tunnelling and geotechnics: New horizons. *Géotechnique, 58*(9), 695–736.

Martinelli, M., Rohe, A., & Soga, K. (2017). Modeling dike failure using the material point method. *Procedia Engineering, 175*, 341–348.

MathWorks. (2023). *MATLAB software v. 2023b*. https://www.mathworks.com.

Meguid, M. A., & Dang, H. K. (2009). The effect of erosion voids on existing tunnel linings. *Tunnelling and Underground Space Technology, 24*(3), 278–286.

Ministry of Housing and Urban-Rural Development. (2014). *GB 50911—2013: Code for monitoring measurement of urban rail transit engineering*. China Building Industry Press.

Ng, C. W. W., Jia, Z. Y., Poudyal, S., Bhatta, A., & Liu, H. M. (2024). Two-phase MPM modelling of debris flow impact against dual rigid barriers. *Géotechnique, 74*(12), 1390–1403.

Pallett, P., Gorst, N., Clark, L., & Thomas, D. (2002). Friction resistance in temporary works materials. *Concrete, 36*(6), 12–15.

Pardo, G. S., & Sáez, E. (2014). Experimental and numerical study of arching soil effect in coarse sand. *Computers and Geotechnics, 57*, 75–84.

Plizzari, G. A., & Tiberti, G. (2006). Steel fibers as reinforcement for precast tunnel segments. *Tunnelling and Underground Space Technology, 21*(3), 438–439.

Qin, X. G., Zhang, G. Z., & Ge, R. Y. (2022). Effect of erosion void on segmental tunnel lining: 2D numerical investigation. *Transportation Geotechnics, 35*, 100792.

Rabczuk, T., & Belytschko, T. (2004). Cracking particles: A simplified meshfree method for arbitrary evolving cracks. *International Journal for Numerical Methods in Engineering, 61*(13), 2316–2343.

Rabczuk, T., Zi, G., Bordas, S., & Nguyen-Xuan, H. (2010). A simple and robust three-dimensional cracking-particle method without enrichment. *Computer Methods in Applied Mechanics and Engineering, 199* (37–40), 2437–2455.

Soga, K., Alonso, E., Yerro, A., Kumar, K., & Bandara, S. (2016). Trends in large-deformation analysis of landslide mass movements with particular emphasis on the material point method. *Géotechnique, 66* (3), 248–273.

Sulsky, D., Zhou, S. J., & Schreyer, H. L. (1995). Application of a particle-in-cell method to solid mechanics. *Computer Physics Communications, 87*(1–2), 236–252.

Sun, Z. Z., Zhang, Y. M., Yuan, Y., & Mang, H. A. (2019). Stability analysis of a fire-loaded shallow tunnel by means of a thermo-hydro-chemo-mechanical model and discontinuity layout optimization. *International Journal for Numerical and Analytical Methods in Geomechanics, 43*(16), 2551–2564.

Tan, Y., & Lu, Y. (2017). Forensic diagnosis of a leaking accident during excavation. *Journal of Performance of Constructed Facilities, 31*(5), 04017061.

Vermeer, P. A., Yuan, Y. X., Beuth, L., & Bonnier, P. (2009). Application of interface elements with the Material Point Method. In *Proceedings of the 18th International Conference on Computer Methods Mechanics*. 18–21 May 2009, Zielona Góra, Poland.

Wallis, S. (2002). Rebuilding the red line at st petersburg. *Tunnels and Tunnelling International, 34*(1), 30–32.

Wang, J. F., Huang, H. W., Xie, X. Y., & Bobet, A. (2014). Void-induced liner deformation and stress redistribution. *Tunnelling and Underground Space Technology, 40*, 263–276.

Wang, L. B., Zhang, C. P., Li, Y. J., Peng, H., Fu, P. J., Jin, Z. X., & Li, W. (2024). Study on dynamic and failure characteristics of sand and anti-floating safety of tunnel structures under long-term vibration loads of the Beijing subway. *Engineering Failure Analysis, 163*, 108591.

Wang, Z. N., & Wang, G. (2023). A coupled MPM and CBFEM framework for large deformation simulation of porous media interacting with pore and free fluid. *Computers and Geotechnics, 163*, 105746.

Wongsaroj, J., Soga, K., & Mair, R. J. (2007). Modelling of long-term ground response to tunnelling under St James's Park. *London. Géotechnique, 57*(1), 75–90.

Wu, H. N., Shen, S. L., Chen, R. P., & Zhou, A. N. (2020). Three-dimensional numerical modelling on localised leakage in segmental lining of shield tunnels. *Computers and Geotechnics, 122*, 103549.

Wu, H. N., Huang, R. Q., Sun, W. J., Shen, S. L., Xu, Y. S., Liu, Y. B., & Du, S. J. (2014). Leaking behavior of shield tunnels under the Huangpu River of Shanghai with induced hazards. *Natural Hazards, 70*(2), 1115–1132.

Xie, X. C., Ceccato, F., Zhou, M. L., & Zhang, D. M. (2022). Hydro-mechanical behaviour of soils during water-soil gushing in shield tunnels using MPM. *Computers and Geotechnics, 145*, 104688.

Yang, F., Cao, S. R., & Qin, G. (2020). Simplified spring models for concrete segmental lining longitudinal joints with gaskets. *Tunnelling and Underground Space Technology, 96*, 103227.

Yang, J., Yin, Z. Y., Laouafa, F., & Hicher, P. Y. (2022). Numerical analysis of internal erosion impact on underground structures: Application to tunnel leakage. *Geomechanics for Energy and the Environment, 31*, 100378.

Ye, Z., & Liu, H. B. (2020). Modeling the effects of internal erosion on the structural damage of a shield tunnel. *International Journal of Geomechanics, 20*(6), 04020053.

Ye, Z., & Liu, H. B. (2021). Investigating the relationship between erosion-induced structural damage and lining displacement parameters in shield tunnelling. *Computers and Geotechnics, 133*, 104041.

Yoo, C. (2017). Effect of water leakage in tunnel lining on structural performance of lining in subsea tunnels. *Marine Georesources and Geotechnology, 35*(3), 305–317.

Zhang, D. M., Phoon, K. K., Hu, Q. F., & Huang, H. W. (2018). Nonlinear subgrade reaction solution for circular tunnel lining design based on mobilized strength of undrained clay. *Canadian Geotechnical Journal, 55*(2), 155–170.

Zhang, D. M., Zhang, X. L., & Du, W. W. (2022). DEM-FEM based numerical analysis on mechanical responses of sandy soil and pipeline to seepage erosion. *Engineering Geology, 310*, 106868.

Zhang, D. M., Du, W. W., Peng, M. Z., Feng, S. J., & Li, Z. L. (2020a). Experimental and numerical study of internal erosion around submerged defective pipe. *Tunnelling and Underground Space Technology, 97*, 103256.

Zhang, D. M., Gao, C. P., & Yin, Z. Y. (2019). CFD-DEM modeling of seepage erosion around shield tunnels. *Tunnelling and Underground Space Technology, 83*, 60–72.

Zhang, D. M., Huang, Z. K., Yin, Z. Y., Ran, L. Z., & Huang, H. W. (2017). Predicting the grouting effect on leakage-induced tunnels and ground response in saturated soils. *Tunnelling and Underground Space Technology, 65*, 76–90.

Zhang, D. M., Ma, L. X., Zhang, J., Hicher, P. Y., & Juang, C. H. (2015a). Ground and tunnel responses induced by partial leakage in saturated clay with anisotropic permeability. *Engineering Geology, 189*, 104–115.

Zhang, D. M., Xie, X. C., Zhou, M. L., Huang, Z. K., & Zhang, D. M. (2021). An incident of water and soil gushing in a metro tunnel due to high water pressure in sandy silt. *Engineering Failure Analysis, 121*, 105196.

Zhang, D. M., Zhang, X. L., & Du, W. W. (2024). Experimental study on interaction mechanism between pipeline seepage erosion and adjacent foundation pile. *Acta Geotechnica, 19*(4), 1745–1763.

Zhang, W. X., De Corte, W., Liu, X., & Taerwe, L. (2020b). Influence of rotational stiffness modeling on the joint behavior of quasi-rectangular shield tunnel linings. *Applied Sciences, 10*(23), 8396.

Zhang, X., Sze, K. Y., & Ma, S. (2006). An explicit material point finite element method for hyper-velocity impact. *International Journal for Numerical Methods in Engineering, 66*(4), 689–706.

Zhang, Y. M., Gao, Z. R., Li, Y. Y., & Zhuang, X. Y. (2020c). On the crack opening and energy dissipation in a continuum based disconnected crack model. *Finite Elements in Analysis and Design, 170*, 103333.

Zhang, Y. M., Lackner, R., Zeiml, M., & Mang, H. A. (2015b). Strong discontinuity embedded approach with standard SOS formulation: Element formulation, energy-based crack-tracking strategy, and validations. *Computer Methods in Applied Mechanics and Engineering, 287*, 335–366.

Zhang, Y. M., & Mang, H. A. (2020). Global cracking elements: A novel tool for Galerkin-based approaches simulating quasi-brittle fracture. *International Journal for Numerical Methods in Engineering, 121*(11), 2462–2480.

Zhang, Y. M., & Zhuang, X. Y. (2018). Cracking elements: A self-propagating strong Discontinuity embedded Approach for quasi-brittle fracture. *Finite Elements in Analysis and Design, 144*, 84–100.

Zhang, Y. M., & Zhuang, X. Y. (2019). Cracking elements method for dynamic brittle fracture. *Theoretical and Applied Fracture Mechanics, 102*, 1–9.

Zhao, Y. D., Choo, J., Jiang, Y. P., & Li, L. C. (2023). Coupled material point and level set methods for simulating soils interacting with rigid objects with complex geometry. *Computers and Geotechnics, 163*, 105708.

Zheng, G., Dai, X., Diao, Y., & Zeng, C. F. (2016). Experimental and simplified model study of the development of ground settlement under hazards induced by loss of groundwater and sand. *Natural Hazards, 82*, 1869–1893.

Zheng, G., Lu, P., & Diao, Y. (2015). Advance speed-based parametric study of greenfield deformation induced by EPBM tunneling in soft ground. *Computers and Geotechnics, 65*, 220–232.

Zheng, X. C., Seaid, M., Pisanò, F., Hicks, M. A., Vardon, P. J., Huvaj, N., & Osman, A. S. (2023). A material point/finite volume method for coupled shallow water flows and large dynamic deformations in seabeds. *Computers and Geotechnics, 162*, 105673.